Coherent Control of a Nuclear Spin via Interactions with a Rare-Earth Ion in the Solid State

Mehmet T. Uysal,[1,†] Mouktik Raha,[1,†,‡] Songtao Chen,[1,§] Christopher M. Phenicie,[1,¶] Salim Ourari,[1] Mengen Wang,[2] Chris G. Van de Walle,[2] Viatcheslav V. Dobrovitski,[3,4] and Jeff D. Thompson[1,*]

[1] *Department of Electrical and Computer Engineering, Princeton University, Princeton, New Jersey 08544, USA*
[2] *Materials Department, University of California, Santa Barbara, California 93106-5050, USA*
[3] *QuTech, Delft University of Technology, Delft 2628 CJ, Kingdom of the Netherlands*
[4] *Kavli Institute of Nanoscience, Delft University of Technology, Delft 2628 CJ, Kingdom of the Netherlands*

(Received 21 September 2022; revised 12 January 2023; accepted 3 February 2023; published 1 March 2023)

Individually addressed Er^{3+} ions in solid-state hosts are promising resources for quantum repeaters, because of their direct emission in the telecom band and their compatibility with silicon photonic devices. While the Er^{3+} electron spin provides a spin-photon interface, ancilla nuclear spins could enable multiqubit registers with longer storage times. In this work, we demonstrate coherent coupling between the electron spin of a single Er^{3+} ion and a single $I = 1/2$ nuclear spin in the solid-state host crystal, which is a fortuitously located proton (^{1}H). We control the nuclear spin using dynamical-decoupling sequences applied to the electron spin, implementing one- and two-qubit gate operations. Crucially, the nuclear spin coherence time exceeds the electron coherence time by several orders of magnitude, because of its smaller magnetic moment. These results provide a path toward combining long-lived nuclear spin quantum registers with telecom-wavelength emitters for long-distance quantum repeaters.

DOI: 10.1103/PRXQuantum.4.010323

I. INTRODUCTION

Optically interfaced solid-state atomic defects are promising for realizing quantum technologies; in particular, quantum networks [1] and sensors [2]. In this approach, the optical transition of the defect provides a direct interface to the electron spin [3]. However, enhanced functionality can be realized by coupling the electron spin to one or more ancillary nuclear spins in the surrounding environment [4,5]. For example, in NV centers in diamond, this approach has been used to realize long-lived nuclear spin quantum registers [6,7], distribute entangled states across a quantum network [8], and implement multiqubit operations such as quantum error-correction protocols [9–12].

Individually addressed rare-earth ions (REIs) are an emerging platform [14–19] with several attractive features, including demonstrated single-shot spin readout [20,21] and subwavelength addressing and control of many defects [22]. They can also be incorporated into a range of materials [23–25], which allows engineering of their environment to improve coherence and integration with devices [17,18,26]. Among REIs, Er^{3+} is particularly promising because its telecom-wavelength (1.5-μm) optical transition may enable long-distance quantum repeaters without frequency conversion. Recent work has made considerable progress on reducing optical spectral diffusion [19], including the demonstration of indistinguishable single-photon emission [27].

REIs are most commonly doped into yttrium-based host materials [28] [e.g., Y_2SiO_5 (YSO), YVO_4, or $Y_3Al_5O_{12}$], which are magnetically noisy, harboring nuclear spins from Y (^{89}Y, with 100% abundance) and other elements (e.g., ^{29}Si in YSO with 4.7% abundance). These form a bath that decoheres the electron spin. Recently, coupling between an REI electron spin (Ce^{3+}) and individual nuclear spins in the bath (^{89}Y, ^{29}Si) has been observed in Ce:YSO [29]. Additionally, coherent coupling and quantum gate operations have been demonstrated between

*jdthompson@princeton.edu
†These authors contributed equally to this work.
‡Present address: Pritzker School of Molecular Engineering, The University of Chicago, Chicago, Illinois 60637, USA
§Present address: Department of Electrical and Computer Engineering, Rice University, Houston, Texas 77005, USA
¶Present address: Fathom Radiant, Boulder, Colorado 80301, USA

a single $^{171}Yb^{3+}$ electron spin and collective states of a small ^{51}V nuclear spin ensemble in Yb:YVO_4 [30]. However, coherent control of a nuclear spin qubit with a coherence time longer than the electron spin has not yet been demonstrated in REIs.

In this work, we demonstrate coherent coupling between the electron spin of a single Er^{3+} ion in YSO to a single nearby nuclear spin. The nuclear spin is controlled via microwave-driven dynamical-decoupling (DD) sequences on the electron spin, realizing one-qubit and two-qubit gate operations that let us probe the coupling strength and coherent dynamics of the nuclear spin. We observe a nuclear-spin T_2 time (with a Hahn echo) of 1.9 ms, about 3 orders of magnitude longer than the same quantity in the Er^{3+} electron spin alone. With a SWAP operation, we also demonstrate that the state of the nuclear spin in the computational basis survives electron-spin readout and reinitialization—an important step toward preserving the full quantum state [31,32]. The properties of the nuclear spin suggest that it is a fortuitously located proton (^1H), the location of which we determine by measuring the coupling strength for several magnetic field configurations. This work adds a key component to the toolkit of individually addressed REIs and also demonstrates a potentially powerful approach to engineering nuclear-spin ancillas using non-native atomic species.

II. RESULTS

Our experimental platform consists of a silicon nanophotonic cavity (PC) bonded to a single-crystal sample of YSO with a trace concentration of Er^{3+} ions [Fig. 1(a)]. The cavity serves to enhance the emission rate [17] and the cyclicity of the Er^{3+} optical transitions, enabling single-shot spin readout [20]. Additionally, microwave fields from a nearby antenna are used to drive spin rotations with a π-pulse duration of approximately 31 ns. Additional details about the experimental geometry can be found in Ref. [33].

In a magnetic field, the spin-1/2 ground and excited states of the Er^{3+} ion become nondegenerate, giving rise to four distinct optical transitions (*A*-*D*) that can be used to control and measure the electron spin [Fig. 1(b)]. We initialize the spin by alternately exciting the ion on the *A* transition and applying microwave π pulses to the excited state, which polarizes the spin into $|\downarrow\rangle$ [22]. Spin readout is accomplished by repeatedly exciting the *B* transition, with a typical single-shot fidelity of 81%. In this work, all of the reported measurement outcomes are normalized by the measurement fidelity to produce an estimate of the true spin population.

We probe the local magnetic environment of the Er^{3+} ion by performing microwave-driven DD sequences [$XY-N := (\tau - \pi_{x/y} - \tau)^N$] on the Er^{3+} spin with varying interpulse separation 2τ [34–36]. On top of an overall coherence decay arising from the nuclear spin bath ($T_{2,XY16} = 16.1 \pm 0.2$ μs), the particular Er^{3+} ion studied in this work exhibits a sharp resonance at $2\tau_0 = 0.875$ μs [Fig. 1(c)]. At the resonance, varying the number of π pulses N in the XY-N sequence yields coherent oscillations of the Er^{3+} spin population [Figs. 1(d) and 1(e)]. We attribute these features to a coherent interaction between the Er^{3+} electron spin and a nearby nuclear spin.

To understand this phenomenon, we consider the interaction Hamiltonian between the electron spin and nuclear spins in the rotating frame of the electron spin under the secular approximation:

$$H/\hbar = 2S_z(A_{||}I_z + A_\perp I_x) + \omega_L I_z. \quad (1)$$

Here, **S** is the pseudo-spin-1/2 operator for the lowest Kramers-doublet electron state, **I** is the nuclear spin operator, $A_{||}$ and $A_\perp$ are parallel and perpendicular hyperfine coupling parameters, and $\omega_L = \gamma_N B/\hbar$ is the (bare) Larmor frequency of the nuclear spin. In the spin Hamiltonian, we define the $\hat{\mathbf{z}}$ axis to be the direction of the external magnetic field, while the $\hat{\mathbf{x}}$ axis is fixed by $A_\perp$. The orientation of the field in the reference frame of the YSO crystal axes is specified in Fig. 1. Rearranging terms in Eq. (1), the Hamiltonian simplifies to

$$H/\hbar = |\uparrow\rangle\langle\uparrow| \otimes \omega_+ \mathbf{I}\cdot\mathbf{m}_+ + |\downarrow\rangle\langle\downarrow| \otimes \omega_- \mathbf{I}\cdot\mathbf{m}_-, \quad (2)$$

where $\omega_\pm = \sqrt{(\omega_L \pm A_{||})^2 + A_\perp^2}$ is the effective Larmor frequency and $\mathbf{m}_\pm = (\pm A_\perp, 0, \pm A_{||} + \omega_L)/\omega_\pm$ is the precession axis of the nuclear spin. From Eq. (2), it is evident that the nuclear spin rotation is conditional on the Er^{3+} electron spin state: it precesses around the $\mathbf{m}_+$ ($\mathbf{m}_-$) axis at the frequency ω_+ (ω_-) when the electron is in the state $|\uparrow\rangle$ ($|\downarrow\rangle$).

In the strong-magnetic-field regime, $\omega_L \gg \sqrt{A_{||}^2 + A_\perp^2}$, $\mathbf{m}_\pm$ are both nearly parallel to the magnetic field axis, $\hat{\mathbf{z}}$. However, the small perpendicular component can be used to generate a conditional rotation of the nuclear spin. Specifically, toggling the electron spin using an XY-N sequence satisfying the resonance condition $2\tau_0 = \pi/\omega_0$ [$\omega_0 = (\omega_+ + \omega_-)/2 \sim \omega_L$] leads to a rotation of the nuclear spin around the effective precession axes $\mathbf{q}_\pm \simeq \pm\hat{\mathbf{x}}$ (Appendix B 1), conditional on the initial electron state [Fig. 1(f)]. After N periods, the evolution of the nuclear spin is described by

$$U_{XY-N} = |\uparrow\rangle\langle\uparrow| \otimes R_x(N\alpha) + |\downarrow\rangle\langle\downarrow| \otimes R_x(-N\alpha), \quad (3)$$

where $\alpha \sim 2A_\perp/\omega_L$ is the rotation angle per π pulse [Fig. 1(e)]. In Fig. 1(c) (inset), we plot the observed resonance frequency of the XY-16 sequence as a function of the magnetic field strength. It exhibits a slope of 4.3 ±

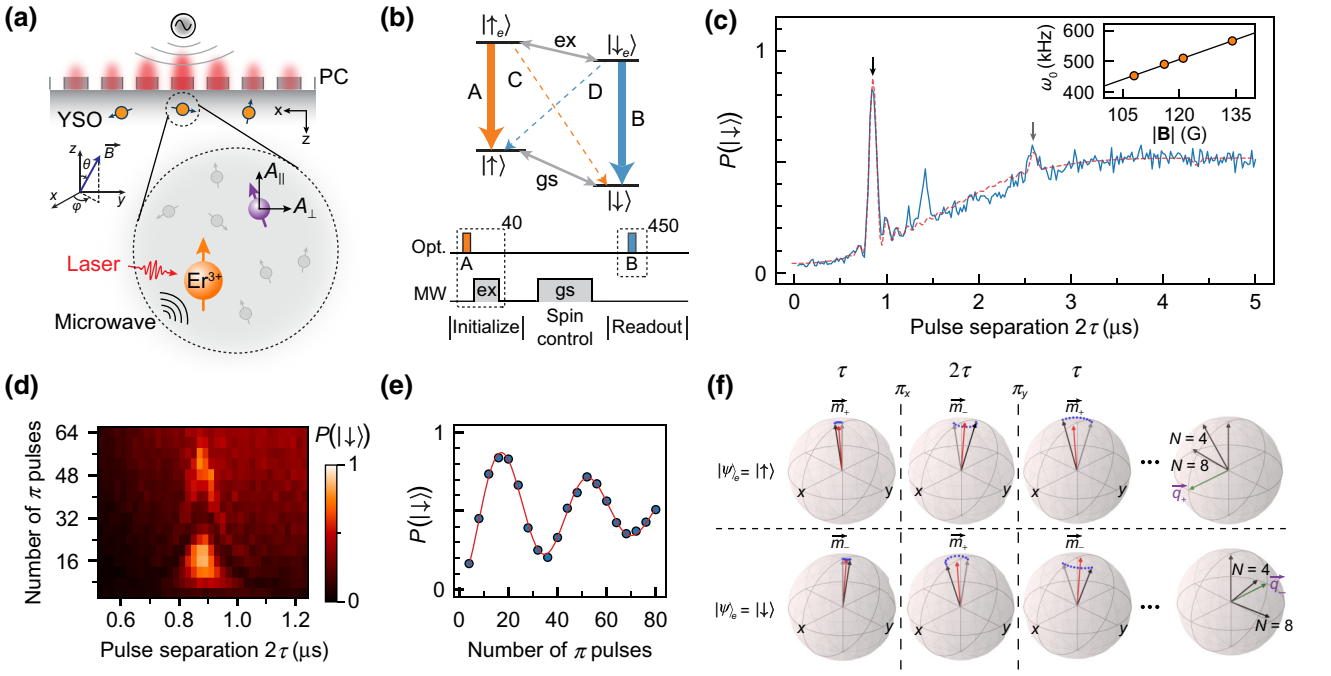

FIG. 1. The detection and coherent control of a weakly coupled nuclear spin using an Er^{3+} electron spin. (a) The measurement scheme. A single Er^{3+} spin, which is initialized, controlled, and read out via a combination of optical and microwave (MW) excitations, probes a nearby nuclear spin. (b) Top, the Er^{3+} level structure; bottom, the pulse scheme for initialization and single-shot readout of the Er^{3+} spin state, interleaved with microwave pulses resonant with the ground-state splitting for spin manipulation. The spin-conserving transitions (labeled "A" and "B") are highly cyclic. (c) The evolution of an Er^{3+} spin under an XY-16 sequence as the separation between consecutive π pulses (2τ) is varied (solid blue curve). The arrows indicate resonances at π/ω_0 and $3\pi/\omega_0$, based on the simulated signal (dashed red line) for the extracted interaction parameters and decay envelope with $T_{2,XY16} = 16.1 \pm 0.2$ μs. The inset shows ω_0 as a function of field-strength fits to a line with slope 4.3 ± 0.1 kHz/G and offset -12 ± 9 kHz. The experiments are performed at field angles $(\theta, \phi) = (90°, 110°)$ and $(90°, 120°)$ in a coordinate system defined by the YSO crystal structure: $(x, y, z) = (D_1, D_2, b)$ [13]. (d) The Er^{3+} spin population plotted as a function of 2τ and the number of π pulses (N) in the XY-N sequence near the resonance centered at $2\tau_0 = 0.875$ μs. The "chevron" interference pattern originates from coherent interaction between the Er^{3+} spin and a nuclear spin. (e) The coherent controlled rotation of the nuclear spin as a function of N at the 2τ resonance position. The data are fitted to a decaying sinusoidal (solid red line) with $\alpha = 10.2°$ rotation per π pulse. (f) The conditional evolution of a nuclear spin based on the Er^{3+} electron spin state for one unit (τ–π_x–2τ–π_y–τ) of our decoupling sequence. Repeating this unit leads to a conditional x rotation of the nuclear spin, around the effective axes $\mathbf{q}_\pm = \pm\hat{\mathbf{x}}$. All of the experiments are performed at the magnetic field configuration $(B, \theta, \phi) = (130\,\mathrm{G}, 95°, 110°)$, corresponding to $(f_{\mathrm{MW,gs}}, f_{\mathrm{MW,ex}}) = (2.02, 1.32)$ GHz, unless indicated otherwise.

0.1 kHz/G, which is consistent with the gyromagnetic ratio of a proton (4.258 kHz/G) within the experimental uncertainty. Using measurement techniques described in Appendix B 3, we can extract the full set of parameters $(|A_{||}|, A_\perp, \omega_L) = (19.4, 50.5, 567.4)$ kHz for the magnetic field orientation used in Figs. 1(c)–1(e). With these parameters, $\alpha = 10.2°$, such that XY-8 approximately implements a maximally entangling conditional-$R_x(\pm\pi/2)$ rotation on the nuclear spin.

We now study the coherence properties of the nuclear spin. Using additional rotations on the electron spin, the conditional-$R_x(\pm\pi/2)$ operation is adapted to a $\mathrm{C}_n\mathrm{NOT}_e$ operation, where the nuclear spin acts as a control [Fig. 2(a)]. The operation is controlled by the nuclear spin state along the $\hat{\mathbf{x}}$ axis, which is roughly perpendicular to the precession axes $\mathbf{m}_\pm$, which are nearly parallel to the $\hat{\mathbf{z}}$ axis. Therefore, the sequence in Fig. 2(a) measures the precession of the nuclear spin states $|\pm x\rangle = (|\uparrow\rangle \pm |\downarrow\rangle)/\sqrt{2}$, equivalent to a standard Ramsey measurement of the nuclear spin coherence (Appendix B 2). The additional π pulse on the electron spin decouples the precession frequency from the (random) initial state of the nuclear spin, so that the average precession frequency ω_0 is observed at short times [Fig. 2(b)]. However, at longer times, the precession shows a complex beating at several frequencies. A fast Fourier transform (FFT) of the Ramsey measurement reveals four symmetrically spaced peaks, where two subgroups of peaks are separated by 14 kHz and each subgroup is split by 4 kHz [Fig. 2(c)]. This suggests the presence of additional spins in the nuclear spin environment, which we discuss below.

We measure the nuclear-spin T_2 with a Hahn-echo sequence, by inserting a π pulse on the nuclear spin during its precession [Fig. 2(d)]. We perform the π pulse

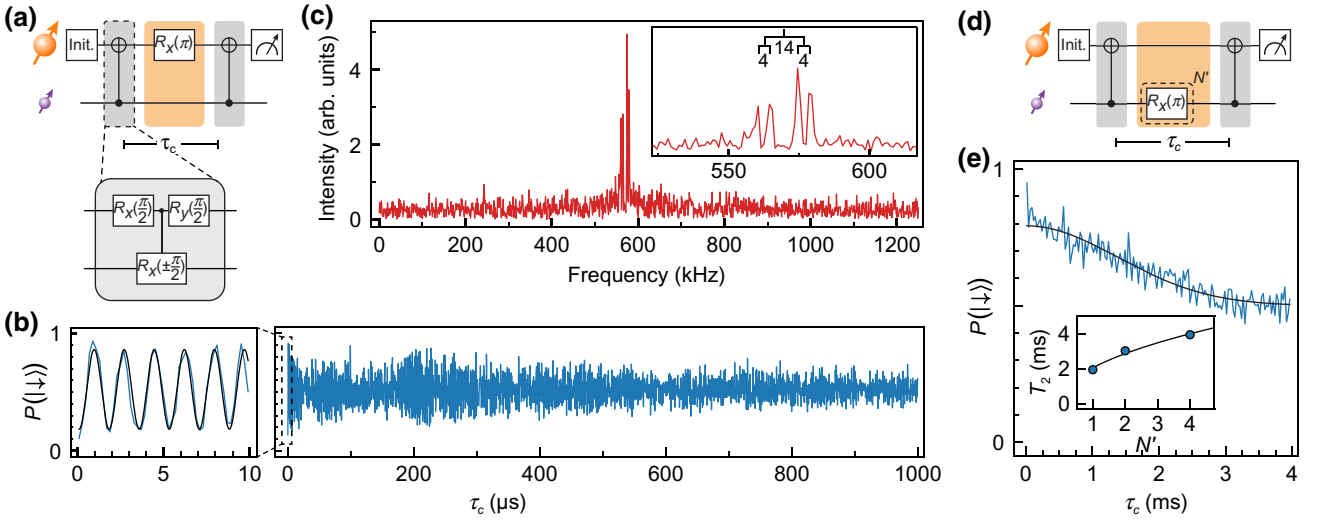

FIG. 2. Probing the nuclear spin coherence. (a) Ramsey spectroscopy of the nuclear spin is performed by changing the delay τ_c between two C_nNOT_e operations and applying a π pulse on the electron at the halfway point. (b) The spectroscopy reveals oscillations at ω_0 in the short time scale (solid black line) and a beating envelope over a millisecond. (c) The FFT of the Ramsey signal reveals four distinct frequency components that are symmetric around ω_0. (d) Hahn and CPMG sequences on the nuclear spin are performed by applying unconditional $R_x(\pi)$ operations. (e) The sequence yields $T_{2,\mathrm{Hahn}} = 1.9 \pm 0.1$ ms and can be extended to $T_{2,\mathrm{CPMG}} = 3.9 \pm 0.2$ ms (inset). The black curve in the inset is a fit to the power function, $T_2 = cN'^k$, with fitted $c = 2.1 \pm 0.2$ ms and $k = 0.5 \pm 0.1$. For further discussion of the nuclear spin coherence, see Appendix E 1.

by applying the conditional-$R_x(\pm\pi/2)$ twice, so that the nuclear spin rotates by π around the $\hat{\mathbf{x}}$ axis regardless of the electron spin state. This cancels the discrete frequency shifts observed in the Ramsey experiment and yields a T_2 time of 1.9 ms, which can be extended to 3.9 ms with repeated applications of the nuclear-spin π pulse in a Carr-Purcell-Meiboom-Gill (CPMG) sequence [Fig. 2(e)]. Crucially, this value is 3 orders of magnitude longer than the bare electron spin coherence ($T_{2,e} =$ 3 μs [22]), demonstrating that the smaller nuclear magnetic moment leads to extended coherence even in the magnetically noisy environment of YSO.

Next, we implement a SWAP operation to store the electronic state in the nuclear spin. The SWAP consists of conditional-$R_x(\pm\pi/2)$ rotations interleaved with single-qubit rotations of the electron spin and $\hat{\mathbf{z}}$ rotations of the nuclear spin, realized via its free precession for duration τ_0 [Fig. 3(a)] (Appendix C 1). To demonstrate the SWAP operation in the computational basis, we perform the following experiment. We first initialize the nuclear spin into the state $|i_n\rangle$ by preparing the electron spin in that state and executing a SWAP. Then, we initialize the electron again in the state $|i_e\rangle$, resulting in the two-qubit state $|i_e i_n\rangle$. To measure that this state is successfully created, we reverse the operation and perform a second SWAP and measure the electron spin to learn i_n (transferring i_e to the nuclear spin) and finally perform a third SWAP and electron-spin measurement to learn i_e.

The populations measured for each two-qubit readout outcome $|m_0 m_1\rangle$, for a given initialization $|i_e i_n\rangle$, yield a SWAP operation fidelity in the computational basis of 87% [Fig. 3(b)]. This fidelity is consistent with a theoretical estimate incorporating the variation of the nuclear-spin precession frequency [Fig. 2(c)], optical excitations of

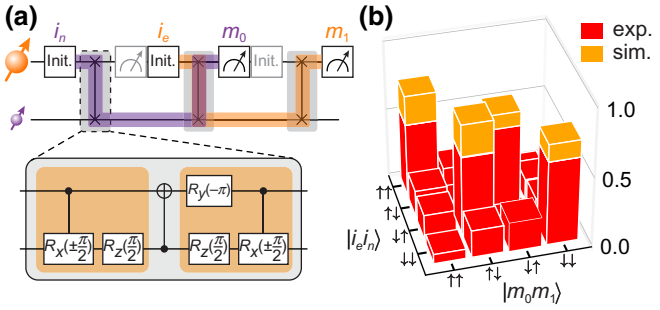

FIG. 3. The SWAP operation. (a) A demonstration of SWAP operations between the electron spin and nuclear spin using the indicated circuit, where the initialization $|i_e\rangle, |i_n\rangle \in \{|\uparrow\rangle, |\downarrow\rangle\}$ corresponds to nuclear-spin and electron-spin initialization due to the action of SWAP. This is followed by readout of $|m_0\rangle$ and $|m_1\rangle$ also interleaved with SWAP. (b) The measurements $|m_0 m_1\rangle$ are plotted for each initialization $|i_e i_n\rangle$. The SWAP pattern is observed as $|i_n\rangle$ ($|i_e\rangle$) determines $|m_0\rangle$ ($|m_1\rangle$), after two SWAP operations. The corresponding SWAP fidelity in the computational basis is 87% (91%) for the experiment (simulation), where the simulation takes into account known error sources. The readout and initialization operations that are not required to explain the operation of SWAP are indicated in gray. We note that the experiment is implemented in a loop structure (see Fig. 6 in Appendix C 3).

the Er^{3+} ion, and a finite lifetime for the nuclear spin (Appendix C 3). This estimate lets us place a lower bound on the intrinsic nuclear-spin lifetime of $T_1 > 0.6$ s. However, the changes in the magnetic moment of the electron spin due to excitations during readout generate significant dephasing of the nuclear spin, which precludes storage of arbitrary nuclear spin states during readout in the current configuration (Appendix C 4).

Finally, we probe the location and gyromagnetic ratio of the nuclear spin in the lattice by measuring the hyperfine parameters $A_{||}$, $A_{\perp}$, and ω_L at four angles of the external magnetic field. The average value of ω_L yields a gyromagnetic ratio $\gamma_N/\hbar = 4.26 \pm 0.04$ kHz/G, which is consistent only with a ^{1}H nuclear spin (4.258 kHz/G). The extracted hyperfine parameters at each field orientation constrain the nuclear-spin position to lie on a one-dimensional manifold. The intersection of these curves (Fig. 4) yields two possible positions of the nuclear spins, which could be further disambiguated by determining the sign of $A_{||}$, which we do not do in this work. For both possible locations, the distance between the electron and the nuclear spin is around 1.9–2 nm (Appendix D). We are not able to confidently assign a position in the YSO crystal structure to the nuclear spin, because of uncertainties in the relative alignment of the magnetic axes of the Er^{3+} site with the crystallographic axes [13], which are not aligned because of the low C_1 symmetry of the Er^{3+} site in YSO.

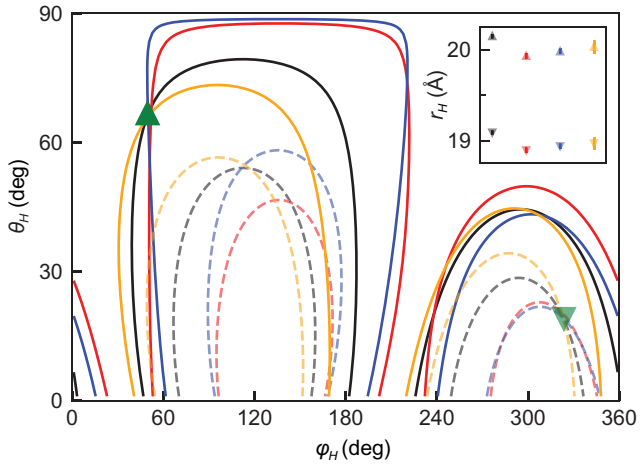

FIG. 4. Locating the nuclear spin. $A_{||}/A_{\perp}$ contour plots, where each contour line (black, red, blue, or orange) corresponds to nuclear-spin positions (θ_H, ϕ_H) that satisfy measurements at magnetic field orientations $(\theta, \phi) = (95, 110)$, (95,140), (85,140), and (100,90), respectively. The intersection of the contour lines, marked by a green triangle, represents a solution. Asserting that $A_{||} > 0$ ($A_{||} < 0$), indicated by solid (dashed) contours, leads to a solution at $\{r_H, \theta_H, \phi_H\} = \{20.0\ \text{Å}, 66.7^\circ, 49.6^\circ\}$ ($\{r_H, \theta_H, \phi_H\} = \{19.0\ \text{Å}, 19.0^\circ, 323.6^\circ\}$). The inset shows calculated distances given $A_{||} > 0$ ($A_{||} < 0$) marked by upward (downward) triangles for each orientation at the indicated solution along with error bars obtained from a Monte Carlo simulation of measurement uncertainty.

III. DISCUSSION

We now turn to a discussion of several aspects of these results. While hydrogen is not part of the YSO chemical formula, it is a ubiquitous impurity that is present during the growth and postprocessing and is able to be unintentionally incorporated into materials [37–39]. The Er^{3+} center studied in this work is one of six ions that we probe in the same sample and the only one to show a strong hydrogen nuclear spin coupling, which is consistent with a hydrogen concentration in the range of 0.3–3.9 $\times$ 10^{18} cm^{-3} (Appendix D 3), a plausible value [40]. Given that hydrogen is quite mobile in oxides, H atoms are also expected to diffuse easily and form defect complexes with large binding energies [41]. It is also noteworthy that the nuclear-spin precession spectrum [Fig. 2(a)] shows four discrete frequency components. In Appendix E 2, we extend our Ramsey measurements to show that the transitions between these frequencies occur as sudden jumps that can be observed with single-shot measurements, with a correlation time of seconds to minutes.

We rule out global magnetic field fluctuations and interactions with other nearby electron spins, because these would have a much larger impact on the Er^{3+} electron, which we do not observe. However, the jumps could be explained by coupling between the H and additional $I = 1/2$ nuclei, with Ising interaction strengths of 2 and 7 kHz. In contrast to the distinctively large gyromagnetic ratio of the hydrogen nuclear spin, nuclear spins with smaller gyromagnetic ratios may not be directly observed via the electron spin within its finite coherence time (Appendix E 2).

Using comprehensive density-functional-theory (DFT) calculations, we conclude that these coupling strengths cannot be explained by the native nuclei alone (^{89}Y and ^{29}Si). However, analysis of a related YSO sample by glow-discharge mass spectroscopy (GDMS) reveals the presence of several chemical impurities with $I = 1/2$ and parts-per-million concentrations, including Cd and P. Typically, both interstitial hydrogen (H_i) and substitutional hydrogen (H_O) tend to act as donors in oxides and are hence attracted to Cd_Y and P_O, which act as acceptors, which may favor the formation of complexes of these impurities despite their low concentration. This hypothesis is further supported by comprehensive DFT calculations: a Cd_Y-H_O complex and a P_O-H_i complex, together with a nearby ^{29}Si, yield coupling strengths to H that are similar to the experimental values [the structures and computational details are included in (Appendix E 3)]. Although the observation of such a nuclear-spin-defect complex is not conclusive at this point, the possibility of engineering nuclear spin

registers using this approach is potentially attractive and could be investigated further.

IV. OUTLOOK AND CONCLUSIONS

Lastly, we consider the prospects for several extensions to this work. First, extension of these techniques to multiple nuclear spins would require the use of phase-controlled rf pulses, which directly drive the nuclear spins, interleaved within DD pulses on the electron spin [42,43]. Such pulse sequences utilize the distinct parallel hyperfine coupling strength of each nuclear spin and are readily applicable for selectively addressing multiple nuclear spins of the same species. In host materials other than YSO, where the abundance of host nuclear spins can be made very small [27,44], this approach may also be used with native nuclear spins. Second, to use the nuclear spin as an ancilla in a quantum network, it is necessary to preserve an arbitrary quantum state during a measurement of the electron spin, as demonstrated with NV centers in diamond [31]. For our platform, the challenge is to preserve the nuclear-spin phase coherence during an optical excitation of the Er^{3+} electron spin, where the nuclear spin accumulates an unknown phase over the long optical lifetime ($T_{1,\mathrm{op}} \simeq 60\ \mu\mathrm{s}$) because of the random timing of spontaneous emission. This can be addressed by minimizing the frequency shift of the nuclear spin when the electron is excited to the excited state, either through alignment of the magnetic field, using more weakly coupled nuclear spins, or encoding information in a decoherence-protected subspace of a pair of nuclear spins [32]. In addition, achieving a shorter excited-state lifetime using higher-quality-factor PC cavities as well as improved electron spin coherence in magnetically quiet host materials [24,25,44] would facilitate all of these future extensions.

In conclusion, we demonstrate coherent interaction between a single Er^{3+} electron spin and a nuclear spin. Using single- and two-qubit operations based on DD sequences, we measure the coherence of this nuclear spin to be several orders of magnitude longer than that of the electron spin. We further show that the nuclear spin state survives the initialization and readout of the electron in the computational basis by implementing a SWAP operation and, finally, we determine its location with respect to the Er^{3+} ion. Together with our previous work on parallel measurement and control of multiple Er^{3+} ions coupled to the same nanophotonic cavity [22], this work is a significant step toward hybrid quantum registers comprised of many telecom-compatible optically interfaced solid-state spins with single-particle control at each node, where each spin is individually coupled to long-lived nuclear spin registers.

ACKNOWLEDGMENTS

We acknowledge helpful conversations with Nathalie de Leon. We acknowledge support from the Air Force Office of Scientific Research (AFOSR) Young Investigator Program (YIP) (FA9550-18-1-0081), the Defense Advanced Research Projects Agency (DARPA) Driven and Nonequilibrium Quantum Systems (DRINQS) program (D18AC00015), and a Department of Energy (DOE) Early Career award (Award No. DE-SC0020120, supporting theoretical modeling). V.V.D. acknowledges support from the DARPA DRINQS program (contract D18AC00015KK1934), as well as the Dutch Research Council (NWO) research program QuTech Physics Funding (QTECH, program 172) with Project No. 16QTECH02, which is (partly) financed by the Dutch Research Council (NWO) and the Kavli Institute of Nanoscience Delft. For the first-principles calculations, M. W. and C. G. VdW. acknowledge support from the U.S. Department of Energy, Office of Science, National Quantum Information Science Research Centers, Co-design Center for Quantum Advantage (C2QA) under Contract No. DE-SC0012704; computational resources were provided by the National Energy Research Scientific Computing Center, a DOE Office of Science User Facility supported by the Office of Science of the DOE, under Contract No. DE-AC02-05CH11231.

APPENDIX A: DEVICE PARAMETERS

The silicon nanophotonic cavity used in this work has a measured quality factor $Q = 4.4 \times 10^4$ and a one-way coupling efficiency $\eta_{\mathrm{cav}} = \kappa_{\mathrm{wg}}/(\kappa_{\mathrm{wg}} + \kappa_{\mathrm{int}}) = 0.19$, where κ_{wg} and κ_{int} are the waveguide and internal loss channels from the cavity, respectively. The particular Er^{3+} ion studied in this work has an optical excited-state lifetime of around 60 μs (corresponding to a Purcell factor of about 190). Further details about the experimental setup and device fabrication can be found in Refs. [22,33].

APPENDIX B: ELECTRON-NUCLEUS HYPERFINE INTERACTION

1. Theoretical background

As stated in the main text, the two-body system of an electron spin and a nuclear spin is described by the secular hyperfine-interaction Hamiltonian in the rotating frame of the electron spin, $H = 2S_z(A_{||} + A_{\perp}) + \omega_L I_z$ (where we set $\hbar = 1$ in the appendix text). We can also express the interaction Hamiltonian in terms of nuclear spin Hamiltonians $H_{\pm}$, which are conditioned on the electron spin state as

$$\begin{aligned} H &= |\uparrow\rangle\langle\uparrow| \otimes H_+ + |\downarrow\rangle\langle\downarrow| \otimes H_-, \\ H_{\pm} &= \omega_{\pm}\mathbf{I}\cdot\mathbf{m}_{\pm} = (\pm A_{||} + \omega_L)I_z \pm A_{\perp}I_x, \end{aligned} \tag{B1}$$

where $\mathbf{m}_{\pm} = (\pm A_{\perp}, 0, \pm A_{||} + \omega_L)/\omega_{\pm}$ and $\omega_{\pm} = \sqrt{(\omega_L \pm A_{||})^2 + A_{\perp}^2}$. A DD sequence can then be described

by periods of free evolution under this Hamiltonian [Eq. (B1)] interleaved with periodically spaced π pulses. A free-evolution propagator for duration τ is given by $U = e^{-iH\tau} = \exp(-i\,|\uparrow\rangle\langle\uparrow| \otimes H_+\tau)\exp(-i\,|\downarrow\rangle\langle\downarrow| \otimes H_-\tau)$. Expanding each exponential yields an intuitive simplification, expressing the nuclear-spin evolution in terms of the Hamiltonians $H_\pm$ conditional on the electron spin state:

$$\begin{aligned} U &= |\uparrow\rangle\langle\uparrow| \otimes e^{-iH_+\tau} + |\downarrow\rangle\langle\downarrow| \otimes e^{-iH_-\tau} \\ &= |\uparrow\rangle\langle\uparrow| \otimes U_+ + |\downarrow\rangle\langle\downarrow| \otimes U_- \\ &= |\uparrow\rangle\langle\uparrow| \otimes e^{-i\phi_+\mathbf{m}_+\cdot\mathbf{I}} + |\downarrow\rangle\langle\downarrow| \otimes e^{-i\phi_-\mathbf{m}_-\cdot\mathbf{I}}. \end{aligned} \tag{B2}$$

As noted above, it is convenient to write the conditional free evolution of the nuclear spin, $U_\pm = e^{-iH_\pm\tau}$, as a rotation around the axes $\mathbf{m}_\pm$ by an angle $\phi_\pm = \omega_\pm\tau$ and express the DD sequence in terms of nuclear spin rotations. Evolution under the basic building block $(\tau\text{–}\pi\text{–}\tau)$ of the DD sequence can be obtained from the free-evolution propagator and the π pulse $X \otimes I$, which acts only on the electron spin, as

$$\begin{aligned} V &= U(X \otimes I)U \\ &= |\uparrow\rangle\langle\downarrow| \otimes U_+U_- + |\downarrow\rangle\langle\uparrow| \otimes U_-U_+ \\ &= |\uparrow\rangle\langle\downarrow| \otimes V_+ + |\downarrow\rangle\langle\uparrow| \otimes V_- \\ &= |\uparrow\rangle\langle\downarrow| \otimes e^{-i\phi\mathbf{n}_+\cdot\mathbf{I}} + |\downarrow\rangle\langle\uparrow| \otimes e^{-i\phi\mathbf{n}_-\cdot\mathbf{I}}. \end{aligned} \tag{B3}$$

Similar to the free-propagation operators, $U_\pm$, we can express the product of rotations $V_\pm = U_\pm U_\mp$ of the nuclear spin as a rotation around an axis $\mathbf{n}_\pm$ by an angle ϕ. However, it is more convenient to work with a repetition of this block $(\tau\text{–}\pi\text{–}2\tau\text{–}\pi\text{–}\tau)$, which is composed of two π pulses and diagonalized in the electron spin basis:

$$\begin{aligned} W &= V^2 = |\uparrow\rangle\langle\uparrow| \otimes V_+V_- + |\downarrow\rangle\langle\downarrow| \otimes V_-V_+ \\ &= |\uparrow\rangle\langle\uparrow| \otimes W_+ + |\downarrow\rangle\langle\downarrow| \otimes W_- \\ &= |\uparrow\rangle\langle\uparrow| \otimes e^{-i(2\alpha)\mathbf{q}_+\cdot\mathbf{I}} + |\downarrow\rangle\langle\downarrow| \otimes e^{-i(2\alpha)\mathbf{q}_-\cdot\mathbf{I}}. \end{aligned} \tag{B4}$$

Continuing the pattern of effective rotation, we express $W_\pm = V_\pm V_\mp$ as a rotation around the axes $\mathbf{q}_\pm$ by an angle 2α. This form has the advantage that any DD sequence $(\tau\text{–}\pi\text{–}2\tau\text{–}\pi\text{–}\tau)^{N/2}$ with an even number of π pulses, N, can be easily expressed as follows:

$$V^N = |\uparrow\rangle\langle\uparrow| \otimes e^{-i(N\alpha)\mathbf{q}_+\cdot\mathbf{I}} + |\downarrow\rangle\langle\downarrow| \otimes e^{-i(N\alpha)\mathbf{q}_-\cdot\mathbf{I}}. \tag{B5}$$

The aforementioned effective rotation axes and angles can be calculated using the identity $e^{-ia_1(\mathbf{p}_1\cdot\boldsymbol{\sigma})}e^{-ia_2(\mathbf{p}_2\cdot\boldsymbol{\sigma})} = e^{-ia(\mathbf{p}\cdot\boldsymbol{\sigma})}$ [$\boldsymbol{\sigma}=(\sigma_x,\sigma_y,\sigma_z)$ is the Pauli vector], where $\mathbf{p}$ and a is expressed as follows:

$$\begin{aligned} \cos a &= \cos a_1 \cos a_2 - \sin a_1 \sin a_2(\mathbf{p}_1 \cdot \mathbf{p}_2), \\ \mathbf{p}\sin a &= \sin a_1 \sin a_2(\mathbf{p}_1 \times \mathbf{p}_2) \\ &\quad + \sin a_1 \cos a_2\mathbf{p}_1 + \sin a_2 \cos a_1\mathbf{p}_2. \end{aligned} \tag{B6}$$

In order to obtain a maximally entangling operation, the effective rotation axes $\mathbf{q}_\pm$ must be antiparallel, such that $\mathbf{q}_+ \cdot \mathbf{q}_- = -1$. Based on Eq. (B6), it can be shown that this condition implies $\cos\phi_+/2\cos\phi_-/2 - \sin\phi_+/2\sin\phi_-/2\cos\gamma = 0$, where $\cos\gamma = \mathbf{m}_+ \cdot \mathbf{m}_-$ is the angle between the free-precession axes $\mathbf{m}_\pm$. When the equality holds, we obtain the following precession axes and angles:

$$\begin{aligned} \cos\alpha &= 1 - 2\left(\sin\frac{\phi_+}{2}\sin\frac{\phi_-}{2}\sin\gamma\right)^2, \\ \mathbf{q}_\pm \sin\alpha &= \pm 2\left(\sin\frac{\phi_+}{2}\sin\frac{\phi_-}{2}\sin\gamma\right)\hat{\mathbf{y}} \\ &\quad \times \left(\sin\frac{\phi_+}{2}\cos\frac{\phi_-}{2}\mathbf{m}_+ + \sin\frac{\phi_-}{2}\cos\frac{\phi_+}{2}\mathbf{m}_-\right). \end{aligned} \tag{B7}$$

In the strong-magnetic-field regime, $\omega_L^2 \gg A_{||}^2 + A_\perp^2$, the free-precession axes $\mathbf{m}_\pm$ are almost parallel to each other, such that $\cos\gamma \sim 1$. This leads to a simpler resonant condition $\cos((\phi_+ + \phi_-)/2) = 0$ or $2\tau = (\pi + m2\pi)/\omega_0$, where $\omega_0 = (\omega_+ + \omega_-)/2$. With further simplifications, we obtain the following:

$$\begin{aligned} \alpha \simeq \gamma &= \frac{2A_\perp\omega_L}{\omega_+\omega_-} \sim \frac{2A_\perp}{\omega_L}, \\ \mathbf{q}_\pm &\simeq \pm\left(\hat{\mathbf{x}} + \frac{A_\perp A_{||}}{\omega_L^2}\hat{\mathbf{z}}\right). \end{aligned} \tag{B8}$$

For a geometrical description of the operation, it is worth noting that the amount of rotation per π pulse, α, is simply equal to the angle γ between the free-precession axes $\mathbf{m}_\pm$ in the strong-magnetic-field regime under the resonant conditions. The deviation of the effective rotation axes $\mathbf{q}_\pm$ from the $\hat{\mathbf{x}}$ direction is on the order of $A_{||}A_\perp/\omega_L^2 \sim 10^{-3}$ for our parameter regime, so we simply label the effective axes $\mathbf{q}_\pm = \hat{\mathbf{x}}_\pm$. With this understanding in place, we express the final form of a DD sequence with N pulses as (where $R_x(\theta) = e^{-i\theta\sigma_x/2}$):

$$V^N = |\uparrow\rangle\langle\uparrow| \otimes R_x(N\alpha) + |\downarrow\rangle\langle\downarrow| \otimes R_x(-N\alpha). \tag{B9}$$

2. Description of C_nNOT_e

We provide a brief discussion of the C_nNOT_e operation. Based on the circuit in Fig. 2(a), C_nNOT_e consists of the

entangling operation U_{XY-8} interleaved between two $\pi/2$ pulses on the electron spin:

$$U_{\mathrm{CNOT}} = (R_y(\pi/2)\otimes I)U_{XY-8}(R_x(\pi/2)\otimes I), \tag{B10}$$

where we define $U_{XY-8} = |\uparrow\rangle\langle\uparrow|\otimes R_x(\pi/2) + |\downarrow\rangle\langle\downarrow|\otimes R_x(-\pi/2)$ as described in the main text. It is helpful to rewrite U_{XY-8} as

$$\begin{aligned} U_{XY-8} &= \frac{1}{2\sqrt{2}}\Big((I+Z)\otimes(I-iX)+(I-Z)\otimes(I+iX)\Big) \\ &= \frac{1}{2\sqrt{2}}\Big((I-iZ)\otimes(I+X)+(I+iZ)\otimes(I-X)\Big) \\ &= R_z(\pi/2)\otimes|+\rangle\langle+| + R_z(-\pi/2)\otimes|-\rangle\langle-|, \end{aligned} \tag{B11}$$

which is a z rotation of the electron spin conditional on the nuclear spin state in $\hat{x}$ basis. Finally, combining the $R_{x/y}(\pi/2)$ operations on the electron spin [Eq. (B10)] with U_{XY-8} leads to U_{CNOT}:

$$\begin{aligned} U_{\mathrm{CNOT}} = R_z(\pi/2)R_x(\pi)\otimes|+\rangle\langle+| \\ + R_z(-\pi/2)\otimes|-\rangle\langle-|. \end{aligned} \tag{B12}$$

Importantly, note that the nuclear spin controls in the $\hat{x}$ basis, while the electron spin is flipped in the $\hat{z}$ basis. In the Ramsey experiment [Fig. 2(b)], this implies that the nuclear-spin precession frequency, $\omega_\pm$, after a $\mathrm{C}_n\mathrm{NOT}_e$ depends on the initial nuclear spin state, as expressed in the x basis. As stated in the main text, the additional π pulse on the electron spin during the nuclear-spin free precession decouples this dependence on the nuclear spin state and allows us to extract the average precession frequency ω_0. Measurement of the hyperfine parameters using the $\mathrm{C}_n\mathrm{NOT}_e$ operation is discussed further in Sec. B 3.

3. Measurement of hyperfine-interaction parameters

We can use the above description of effective precession axes to obtain the conditional free-precession frequencies ω_+ and ω_- of the nuclear spin. When combined with the knowledge of α, these three parameters are sufficient to solve for the Hamiltonian parameters ($A_{||}$, $A_\perp$, and ω_L).

However, rather than measuring $\omega_\pm$ directly, we measure $\omega_0 = (\omega_+ + \omega_-)/2$ and $\omega_\delta = (\omega_+ - \omega_-)/2$. To extract ω_0, we perform a Ramsey measurement using the pulse sequence sketched in Fig. 2(a). Here, the nuclear spin undergoes free precession in the interval between two $\mathrm{C}_n\mathrm{NOT}_e$ operations. The additional π pulse on the electron spin during the interval ensures that the effective precession frequency of the nuclear spin is an average of ω_+ and ω_-, i.e., ω_0. We emphasize that the signal from this Ramsey experiment is first-order sensitive to any fluctuations of ω_0, as observed in Fig. 2(c), but the extracted precession frequency can also be used to infer hyperfine parameters, as discussed in this section. To see this analytically, we first consider the free evolution during the experiment in Fig. 2(a) as

$$U_{\pi_e}(\tau_c) = U(\tau_c/2)(X\otimes I)U(\tau_c/2). \tag{B13}$$

Noting that this is equivalent to the unitary operator V for $\tau = \tau_c/2$ in Eq. (B3), we can express it as an effective precession conditional on the electron spin state:

$$\begin{aligned} U_{\pi_e}(\tau_c) = |\uparrow\rangle\langle\downarrow|\otimes e^{-i\phi\mathbf{n}_+\cdot\mathbf{I}} + |\downarrow\rangle\langle\uparrow|\otimes e^{-i\phi\mathbf{n}_-\cdot\mathbf{I}} \\ e^{-i\phi\mathbf{n}_\pm\cdot\mathbf{I}} = e^{-i\phi_\pm\mathbf{m}_\pm\cdot\mathbf{I}}e^{-i\phi_\mp\mathbf{m}_\mp\cdot\mathbf{I}}, \end{aligned} \tag{B14}$$

where the rotation around each free-precession axis, $\mathbf{m}_\pm = (\pm A_\perp, 0, \omega_L \pm A_{||})/\omega_\pm$, is given by $\phi_\pm = \omega_\pm\tau_c/2$. By defining $U_0 = U_{\mathrm{CNOT}}U_{\pi_e}(\tau_c)U_{\mathrm{CNOT}}$ and considering its action on the two-qubit initial state, $\rho_i = |\downarrow\rangle\langle\downarrow|\otimes I/2$, we can compute the signal, $s_0(\tau_c)$, for population measurement on the electron spin to first order in $A_{||}$:

$$\begin{aligned} s_0(\tau_c) = \mathrm{Tr}[U_0\rho_i U_0^\dagger P_\downarrow] \simeq 1 - \cos\frac{\phi}{2}^2 \\ - \left(\frac{A_\perp}{\omega_+\omega_-}\left(\omega_0\sin\frac{\phi_+-\phi_-}{2} + 2A_{||}\sin\frac{\phi_++\phi_-}{2}\right)\right)^2. \end{aligned} \tag{B15}$$

In the strong-magnetic-field regime, where the free-precession axes $\mathbf{m}_\pm$ are approximately parallel, such that $\cos\gamma \sim 1$, Eq. (B6) leads to $\cos\phi/2 = \cos\phi_+/2\cos\phi_-/2 - \sin\phi_+/2\sin\phi_-/2 = \cos(\phi_+ + \phi_-)/2$. This implies that, in this regime, the net rotation will simply be $\phi = \phi_+ + \phi_- = \omega_0\tau_c$. Although the second term in Eq. (B15) also includes frequencies $\omega_\pm/2$ and ω_δ, their magnitude is lower by $(A_\perp/\omega_L)^2 \sim 10^{-2}$. Neglecting this second term, the signal [Eq. (B15)] reduces to $s_0(\tau_c) \simeq 1 - \frac{1}{2}\cos\omega_0\tau_c$.

In order to obtain ω_δ, we insert an additional π pulse on the nuclear spin by using XY-16 operation as described in the main text:

$$U_{\pi_e,\pi_n}(\tau_c) = U(\tau_c/2)(X\otimes X)U(\tau_c/2). \tag{B16}$$

In a similar fashion to Eq. (B14), we can express this operation as a consecutive rotation of the nuclear spin around two axes, one of which is inverted due to the additional π pulse on the nuclear spin:

$$\begin{aligned} U_{\pi_e\pi_n}(\tau_c) = |\uparrow\rangle\langle\downarrow|\otimes e^{-i\phi'\mathbf{n}'_+\cdot\mathbf{I}}X + |\downarrow\rangle\langle\uparrow|\otimes e^{-i\phi'\mathbf{n}'_-\cdot\mathbf{I}}X, \\ e^{-i\phi'\mathbf{n}'_\pm\cdot\mathbf{I}} = e^{-i\phi_\pm\mathbf{m}_\pm\cdot\mathbf{I}}e^{-i\phi_\mp\mathbf{m}'_\mp\cdot\mathbf{I}}, \end{aligned} \tag{B17}$$

where $\mathbf{m}'_\pm = (\pm A_\perp, 0, -(\omega_L \pm A_{||})/\omega_\pm)$ are the inverted axes for the nuclear spin. Defining $U_\delta = U_{\mathrm{CNOT}}U_{\pi_e\pi_n}(\tau_c)$

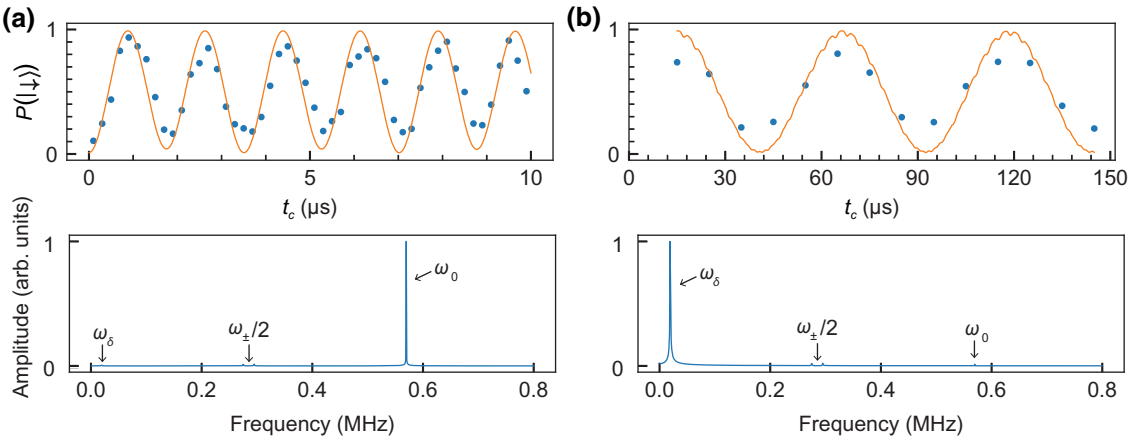

FIG. 5. Observing ω_0 and ω_δ. (a) The simulated $s_0(\tau_c)$ signal overlaid with experimental data and the FFT of the simulation, displaying the peak at ω_0. (b) A similar plot of $s_\delta(\tau_c)$ and its FFT with a peak at ω_δ. The earliest data point in the top panel starts at around 15 μs due to the finite length of the unconditional-$R_x(\pi)$ on the nuclear spin.

U_{CNOT} acting on the same initial state, we also compute the expected signal, $s_\delta(\tau_c)$:

$$s_\delta(\tau_c) = \text{Tr}[U_\delta \rho_i U_\delta^\dagger P_\downarrow] \simeq \cos\frac{\phi'^2}{2} + \left(\frac{A_\perp}{\omega_+\omega_-}\left(\omega_0 \sin\frac{\phi_+ - \phi_-}{2} + 2A_{||}\sin\frac{\phi_+ + \phi_-}{2}\right)\right)^2. \tag{B18}$$

Due to the additional π pulse on the nuclear spin, the two precession axes are approximately antiparallel, such that $\mathbf{m}_\pm \cdot \mathbf{m}'_\mp = \cos\gamma' \sim -1$. Again based on Eq. (B6), this yields $\cos\phi'/2 = \cos\phi_+/2\cos\phi_-/2 + \sin\phi_+/2\sin\phi_-/2 = \cos(\phi_+ - \phi_-)/2$, which implies that $\phi' = \phi_+ - \phi_- = \omega_\delta\tau_c$. Neglecting the second term, Eq. (B18) reduces to $s_\delta(\tau_c) \simeq 1 + \frac{1}{2}\cos\omega_\delta\tau_c$.

The measurement of α [Eq. (B8)], in addition to ω_0 and ω_δ, is sufficient to solve for the parameters $A_{||}$, $A_\perp$, and ω_L. Although the above analysis assumes perfect C_nNOT_e and $R_x(\pi)$ operations on the nuclear spin, we use the exact unitary operators obtained from the hyperfine parameters for XY-8 and XY-16 sequences in simulation (Fig. 5). However, the decoherence mechanisms to be discussed for the SWAP operation are not included in these simulations. Finally, note that the signal $s_\delta(\tau_c)$ is agnostic to the sign of ω_δ, so that the sign of $A_{||}$ is undetermined.

APPENDIX C: SWAP OPERATION AND NUCLEAR-SPIN MEMORY

1. Description of SWAP

We can investigate error sources for the SWAP operation by looking into its constituents. From here on, we use the convention that $|\uparrow\rangle = |0\rangle$ and $|\downarrow\rangle = |1\rangle$ for both the electron spin and nuclear spin bases. As noted in Fig. 3, a SWAP operation can be constructed using a combination of C_nNOT_e and single-qubit rotations, where C_nNOT_e is sketched in Fig. 2(c). Analytically, the SWAP operation can be expressed as

$$\begin{aligned} U_S &= U_{XY-8}(R_y(-\pi/2)\otimes R_z(\pi/2))U_{XY-8} \\ &\quad (R_x(\pi/2)\otimes R_z(\pi/2))U_{XY-8} \\ &= -e^{i\pi/4}(|00\rangle\langle 00| - i|01\rangle\langle 10| - |10\rangle\langle 01| \\ &\quad - i|11\rangle\langle 11|). \end{aligned} \tag{C1}$$

Here, $U_{XY-8} = |0\rangle\langle 0|\otimes R_x(\pi/2) + |1\rangle\langle 1|\otimes R_x(-\pi/2)$ is the conditional-$R_x(\pm\pi/2)$ unitary resulting from the XY-8 sequence [Eq. (B9)]. This can be transformed into an iSWAP gate by using single-qubit $\hat{\mathbf{z}}$ rotations before and after U_S:

$$\begin{aligned} i\text{SWAP} &= (R_z(5\pi/4)\otimes R_z(0))U_S(R_z(\pi)\otimes R_z(\pi/4)) \\ &= |00\rangle\langle 00| + i|01\rangle\langle 10| + i|10\rangle\langle 01| + |11\rangle\langle 11|. \end{aligned} \tag{C2}$$

As the $R_z(\pi/2)$ rotation on the nuclear spin is realized via its free precession, the fidelity of U_S is limited primarily by the T_2^* of the nuclear spin. In particular, the presence of four distinct nuclear-spin precession frequencies, as shown in Fig. 2(c), should be considered when estimating the fidelity of the operation.

2. Description of error channels during the SWAP experiment

The primary sources of error are: (1) modulation of the nuclear-spin precession frequency; and (2) variation in the hyperfine-interaction strength when the electron is in the excited state (during initialization and readout). These can be represented as trace-preserving quantum channels

acting on the two-qubit density matrix, ρ. Accounting for these errors in the SWAP experiment (Fig. 3), we can calculate a lower bound for the nuclear spin T_1.

First, let us incorporate the effects of precession-frequency modulation using a quantum channel description. The basic building block of the SWAP operation is the free evolution of our two-body system for the duration τ_0, realizing both the XY-8 sequence and the $\hat{\mathbf{z}}$ rotation of the nuclear spin. We label the corresponding quantum channel as $S^i_{\tau_0}(\rho)$, where the superscript i indicates that the nuclear spin precesses at one of the four frequencies $\omega_{L,i} = \omega_L + \Delta_i$ ($\Delta_i \in \{\pm 5, \pm 9\}$ kHz), as identified in Fig. 2(c). This basic channel is calculated by evolving ρ under the hyperfine Hamiltonian [Eq. (B1)] and electron-spin dephasing [Fig. 1(c)] for duration τ_0 under the Linblad master equation. Corresponding SWAP channels, $\mathcal{S}^i_{\mathrm{SWAP}}(\rho)$, can be obtained by interleaving $S^i_{\tau_0}(\rho)$ with unitary channels to apply single-qubit rotations on the electron spin as described in Sec. C 1. The final SWAP channel, $\mathcal{S}_{\mathrm{SWAP}}(\rho)$, averages over the four precession frequencies for the nuclear spin:

$$\mathcal{S}_{\mathrm{SWAP}}(\rho) = \frac{1}{4}\sum_{i=1}^{4} \mathcal{S}^i_{\mathrm{SWAP}}(\rho). \tag{C3}$$

On the other hand, errors due to variation in hyperfine-interaction strength can also be accounted for using a similar quantum channel description. The action of a spin-selective excitation pulse can be understood as an infinitesimal sum over unitary operations, corresponding to the variable decay time of the electron from the excited state back to the ground state. First, we give a quantum channel description of the readout scheme sketched in Fig. 1(b). An optical excitation pulse projects the electron spin to the states $|1\rangle$ and $|0\rangle$, via the projectors P_1 and P_0, respectively. If the electron is in the $|1\rangle$ state, it is excited and undergoes a unitary evolution under the excited-state Hamiltonian H^i_e for time t and the ground-state Hamiltonian H^i_g for the remainder of the photon collection window t_W (120 μs), where i denotes the index of $\omega_{L,i}$ in each Hamiltonian. If the electron is in the $|0\rangle$ state, it remains unaffected by the optical excitation and simply evolves under H^i_g for duration t_W. Finally, if the electron has not decayed within this time, it will evolve under H^i_e for duration t_W. As with the SWAP channel [Eq. (C3)], we also consider the variation in the nuclear-spin Larmor frequency, but here we ignore electron-spin dephasing, as the electron is projected to its computational basis after readout. We provide below a definition of the excitation channel, $\mathcal{S}^1_{\mathrm{excite}}(\rho)$, for the $|1\rangle$ transition used in the readout:

$$\begin{aligned}\mathcal{S}^1_{\mathrm{excite}}(\rho) &= S(0, P_0\rho P_0) + p_R S(t_W, P_1\rho P_1) \\ &\quad + \int_0^{t_W} dt p(t) S(t, P_1\rho P_1),\end{aligned}$$

$$\begin{aligned}S(t,\rho) &= \frac{1}{4}\sum_i^4 U^i(t)\rho U^{i\dagger}(t) \\ U^i(t) &= e^{-iH^i_g(t_W-t)}e^{-iH^i_e t}, \\ p(t) &= \frac{1}{T_{1,\mathrm{op}}}e^{-t/T_{1,\mathrm{op}}}, \\ p_R &= 1 - \int_0^{t_W} p(t)dt.\end{aligned} \tag{C4}$$

Note that the excitation channel description for initialization, $\mathcal{S}^0_{\mathrm{excite}}(\rho)$, can be obtained similarly by swapping the projectors P_0 and P_1. We measure the optical lifetime $T_{1,\mathrm{op}}$ (60 μs) in an independent measurement and calculate H^i_e based on the reported g tensor [13] and estimated position for the nuclear spin relative to the Er^{3+} ion (Fig. 4). As discussed in Sec. C 4 with a simple example, in the strong-magnetic-field regime, the effect of the excitation channel is primarily a dephasing of the nuclear spin due to the uncertainty in phase accumulated by the nuclear spin during the excitation and decay of the electron spin.

Using Eq. (C4) as the basic block, we can also construct the full quantum channel description of the readout and initialization processes, consisting of 450 and 40 optical pulses, respectively [Fig. 1(c)]. Importantly, we take into account the finite cyclicity of the optical transition to induce spin flips, $p_f = 0.2\%$ and the excited-state microwave (MW) π pulse during the initialization. This means that the electron spin will only be excited until it is optically pumped to the other spin state.

3. Estimate of nuclear-spin T_1

With the channels described above, we can simulate the SWAP experiment (Fig. 3), consisting of multiple rounds of initialization, SWAP, and readout. To estimate the nuclear-spin T_1, we extract the fidelity of the SWAP from the experiment and compute the same quantity based on our theoretical model. The difference between the two lets us put a lower bound on the nuclear-spin T_1. To extract the fidelity, we consider the initialization i_n and readout m_0, shown in Fig. 3, where the SWAP operation is applied twice for storage and retrieval of the computational basis states $|0\rangle$ ($|\uparrow\rangle$) and $|1\rangle$ ($|\downarrow\rangle$). An important implementation detail is that the steps for initialization, SWAP, and readout are looped multiple times during the experiment. Therefore, Fig. 3 can be equivalently sketched as Fig. 6. The Fig. 3 histogram indices can then be relabeled as $(i_e, i_n) \equiv (i_{k+1}, i_k)$ and $(m_0, m_1) \equiv (m_{k+1}, m_{k+2})$, keeping in mind the modular structure.

After accounting for all known sources of errors described in Sec. C 2, we attribute the remaining difference in simulation and experiment fidelity to the nuclear-spin T_1, as in $F_{\mathrm{exp}} = e^{-T_{\mathrm{store}}/T_1}F_{\mathrm{sim}}$, where $T_{\mathrm{store}} = 59.2$ ms is the time between the initialization i_k and readout m_{k+1},

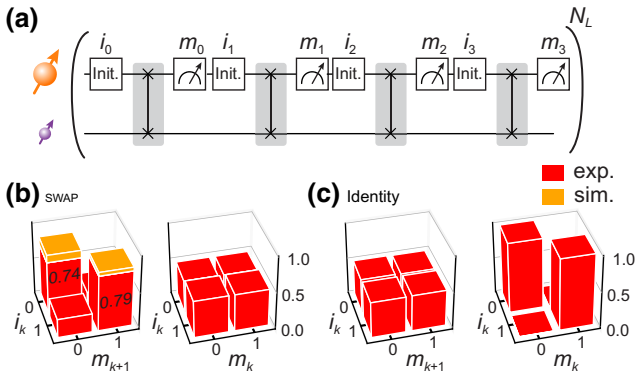

FIG. 6. The SWAP experiment. (a) Implementation of the SWAP experiment, where a SWAP operation is interleaved between each initialization i_k and subsequent readout m_k. A sequence of initialization $(i_0, i_1, i_2, i_3) = (0, 0, 1, 1)$ is repeated $N_L = 1500$ times in a loop, such that all instances $(i_k, i_{k+1}) = \{00, 01, 10, 11\}$ are realized. This allows for all initialization combinations of the electron-nuclear spin pair in the computational basis to be generated. (b) The histogram verifies that the initialization i_k is read out at m_{k+1}, while being uncorrelated with m_k. The average success rate for retrieving the information in experiment (simulation) is 76% (84%). (c) A control experiment, where the SWAP operation is replaced by an identity, shows that i_k is fully correlated with m_k and uncorrelated with m_{k+1}, as expected.

while $F_{\text{exp}} = 0.76$ and $F_{\text{sim}} = 0.84$ are the experiment and simulation fidelities for retrieval of the initialization i_k at m_{k+1}. Attributing this remaining difference to the nuclear-spin lifetime allows us to put a lower bound on the T_1 of 0.63 s. However, the difference could also originate from other sources of error that are not included in the simulations. Finally, considering that the SWAP acts twice during the computation of the fidelities ($F_{\text{exp}}, F_{\text{sim}}$), we can extract a SWAP fidelity in the computational basis of $F_{\text{SWAP,exp}} = 87\%$ and $F_{\text{SWAP},sim} = 91\%$ for the experiment and simulation, respectively.

4. Discussion on storing arbitrary states

Although we demonstrate information storage and retrieval in the computational basis, it is of greater interest to store an arbitrary state in the nuclear-spin memory. To consider this plausibility, we discuss a simple problem of nuclear-spin dephasing under optical excitation of the electron. To obtain a simple analytical expression, we only consider changes in the parallel hyperfine term $A_{||}$, which largely accounts for the dephasing in the strong field regime, using the ground- and excited-state Hamiltonians, $H_g = 2A_g S_z I_z + \omega_L I_z$ and $H_e = 2A_e S_z I_z + \omega_L I_z$, respectively. Limiting ourselves to the subspace where the electron is in the $|1\rangle$ state and moving to a rotating frame of the nuclear spin at $\omega_L - A_g$, we have the nuclear spin Hamiltonians conditional on the electron excitation state:

$$H_g = 0, \quad H_e = \delta_A I_z, \quad \delta_A = A_g - A_e. \tag{C5}$$

Starting with the nuclear spin state in an equal superposition, $|\psi_n\rangle = 1/\sqrt{2}(|0\rangle + |1\rangle)$ (which is most sensitive to dephasing), we can time evolve the state as

$$\begin{aligned}\rho(t) &= |\psi_n(t)\rangle\langle\psi_n(t)| \\ &= \frac{1}{2}(|0\rangle\langle 0| + |1\rangle\langle 1| + e^{i\delta_A t'}|0\rangle\langle 1| + e^{-i\delta_A t'}|1\rangle\langle 0|),\end{aligned} \tag{C6}$$

where the electron was excited at $t = 0$ and is decayed at $t = t'$. Assuming a standard probability distribution for the excited-state decay, $P(t) = \gamma e^{-\gamma t}$, we can calculate the density matrix for the nuclear spin after one decay of the electron as

$$\begin{aligned}\rho_n^{(1)} &= \int_0^\infty dt' P(t')\rho(t') \\ &= \frac{1}{2}(|0\rangle\langle 0| + |1\rangle\langle 1| + c|0\rangle\langle 1| + c^*|1\rangle\langle 0|), \\ c &= \frac{1/\tau}{1/\tau - i\delta_A}.\end{aligned} \tag{C7}$$

The nuclear-spin density matrix after N excitations will simply result from propagating the density matrix through repeated decays in the same manner:

$$\rho_n^{(N)} = \frac{1}{2}(|0\rangle\langle 0| + |1\rangle\langle 1| + c^N|0\rangle\langle 1| + c^{*N}|1\rangle\langle 0|). \tag{C8}$$

Therefore, the purity of the density matrix can be expressed as the length of the Bloch-vector magnitude, where $\delta_f = \delta_A/(2\pi)$:

$$F = \sqrt{2\text{Tr}[\rho_n^{(N)2}] - 1} = \left(\frac{1}{\sqrt{1 + 4\pi^2\delta_f^2/\gamma^2}}\right)^N. \tag{C9}$$

Based on our parameters, $\delta_f/\gamma = 0.56$, the Bloch-vector length for a superposition state, reduces to $F = 0.3$ after a single excitation. In order to achieve $F = 0.9$ after 450 excitations (typically used in single-shot readout), we need $\delta_f/\gamma = 0.0034$. The required factor-of-approximately-150 improvement in the ratio can be plausibly obtained by a combination of using more weakly coupled nuclear spins and choosing a magnetic field direction to minimize δ_f or increasing the decay rate, γ, via stronger Purcell enhancement of the optical transition. As commented in Ref. [13], the Er^{3+} :YSO g tensors for the ground state ($^4I_{15/2}$) and excited state ($^4I_{13/2}$) allow for choosing magnetic field directions such that the interaction of the electron spin with the bath is unperturbed by an excitation. This can then allow information to remain protected in the nuclear spin during a spin-photon entanglement generation attempt that requires repeated excitations of the electron spin.

APPENDIX D: NUCLEAR-SPIN SEARCH

1. Obtaining hyperfine parameters from magnetic dipole Hamiltonian

In order to locate the nuclear spin with respect to the electron, we can study the position dependence of the hyperfine parameters $A_{||}$, $A_{\perp}$, and ω_L. The hyperfine Hamiltonian [Eq. (B1)], expressed in terms of these parameters, can be obtained from the magnetic dipole Hamiltonian between the Er^{3+} spin and the nuclear spin:

$$H_{\rm dip} = -\frac{\mu_0}{4\pi r^3}\mu_B\mu_N g_n \left(\overleftrightarrow{g}\mathbf{S}\cdot\mathbf{I} - 3(\overleftrightarrow{g}\mathbf{S}\cdot\hat{\mathbf{r}})(\mathbf{I}\cdot\hat{\mathbf{r}})\right), \quad \text{(D1)}$$

where μ_B is the Bohr magneton, μ_N is the nuclear magneton, μ_0 is the magnetic permeability, g_n is the nuclear-spin g factor, $\overleftrightarrow{g}$ is the electron-spin g tensor in the solid-state host, r is the distance between the electron spin and nuclear spin, and $\hat{\mathbf{r}}$ is the direction. Under a static magnetic field, each spin also obtains a Zeeman Hamiltonian:

$$H_Z = \mu_B\mathbf{B}\overleftrightarrow{g}\mathbf{S}' - \mu_N g_n\mathbf{B}\cdot\mathbf{I}', \quad \text{(D2)}$$

where the magnetic field vector $\mathbf{B}$ and electron (nuclear) spin vector $\mathbf{S}'$ ($\mathbf{I}'$) are in the laboratory frame. The S_z and I_z operators are defined using these terms:

$$S_z = \mathbf{B}\overleftrightarrow{g}\mathbf{S}'/|\mathbf{B}\overleftrightarrow{g}|, \quad I_z = \mathbf{B}\cdot\mathbf{I}'/|\mathbf{B}|. \quad \text{(D3)}$$

This yields the electron- and nuclear-spin Larmor frequencies as $\omega_{L,e} = \mu_B|\mathbf{B}\overleftrightarrow{g}|$ and $\omega_{L,n} = \mu_N g_n|\mathbf{B}| = \gamma_N|\mathbf{B}|$ (γ_N being the gyromagnetic ratio), yielding $H_Z = \omega_{L,e}S_z + \omega_{L,n}I_z$.

As described in the main text, we work in the frame rotating with $\omega_{L,e}S_z$ and under the secular approximation, such that terms that do not commute with S_z are discarded. The Hamiltonian in Eq. (D1) then reduces to $H_{\rm dip,RWA} = \sum_i 2A_iS_zI_i$, where $A_i = {\rm Tr}[\{H_{\rm dip}, S_zI_i\}]$ can be extracted via anticommutation relations. We can further simplify the interaction terms A_i into $A_{||} = A_z$ and $A_{\perp} = \sqrt{A_x^2 + A_y^2}$, since I_x and I_y operators can always be rotated such that A_y is set to 0 and $A_x \geq 0$. This reduces $H_{\rm dip,RWA}$ to a simple form of $H = 2S_z(A_{||}I_z + A_{\perp}I_x) + \omega_L I_z$, which is provided in the main text and is defined in terms of only three parameters.

Then, the only unknown variables in determining the parameters $A_{||}$, $A_{\perp}$, and ω_L are γ_N, r, and $\hat{\mathbf{r}}$, which tell us the species and location of the nuclear spin. The problem is made simpler by observing that the ratio $A_{||}/A_{\perp}$ only depends on $\hat{\mathbf{r}}$, since both the numerator and denominator of the ratio vary proportionately with γ_N/r^3. γ_N can also be determined independently from the Larmor frequency ω_L. The remaining unknown, r, can then be determined from $\sqrt{A_{||}^2 + A_{\perp}^2}$ values, given $\hat{\mathbf{r}}$ and γ_N. We use this approach to roughly determine the location and constrain the volume considered in the χ^2 calculation to report the most likely position.

2. Determining location

We parametrize the χ^2 calculation in terms of the nuclear-spin location $\mathbf{r}(\equiv r\hat{\mathbf{r}})$ with respect to the Er^{3+} ion. We directly compare the experimental measurements of ω_0, ω_δ, and α, discussed in Sec. B 3, to model estimates of the same measurements as a function of $\mathbf{r}$:

$$\chi^2(\mathbf{r}) = \sum_i \frac{\left(x_{{\rm obs},i} - x_{{\rm mod},i}(\mathbf{r})\right)^2}{\sigma_{{\rm obs},i}^2 + \sigma_{{\rm mod},i}^2(\mathbf{r})}. \quad \text{(D4)}$$

Here, $x_{{\rm obs},i}$ and $x_{{\rm mod},i}$ correspond to the observed and estimated values of ω_0, ω_δ, and α at four different magnetic field orientations, as indicated in Fig. 4, such that there are 12 data points that are compared in total and three parameters, r_H, θ_H, and ϕ_H, to optimize. $\sigma_{{\rm obs},i}$ and $\sigma_{{\rm mod},i}$ correspond to the errors in each data point, where the former arises due to experimental uncertainties and the latter is obtained from Monte Carlo simulations as explained below.

Uncertainty in the model estimates originates from errors in the static magnetic field orientation. We estimate the orientation uncertainty by allowing a shift of the intended field to first order, as in $(B + \Delta B, \theta + \Delta\theta, \phi + \Delta\phi)$, where B is the field magnitude and (θ, ϕ) is the magnetic field orientation with respect to the (D_1, D_2, b) axes of the crystal [13] [Fig. 1(a)]. We choose $(\Delta B, \Delta\theta, \Delta\phi)$ such that the measured splitting for the ground- and excited-state spin levels using optically detected magnetic resonance (ODMR) are minimized with respect to the predicted values at the field settings used. This yields $\Delta B = 3.99 \pm 0.76$ G, $\Delta\theta = 0.89^\circ \pm 0.34^\circ$, and $\Delta\phi = 0.79^\circ \pm 0.44^\circ$. The correction yields a field strength of $B = 134$ G for the four measurements indicated in Fig. 4. Based on the ω_L values obtained at each orientation, we estimate a gyromagnetic ratio γ_N of 42.6 ± 0.4 MHz/T. Since this value is consistent with the hydrogen gyromagnetic ratio, 42.58 MHz/T, we set the hydrogen g factor as a constant in the χ^2 calculations. To calculate the uncertainty in the model estimates, we propagate the uncertainty in the magnetic field, via a Monte Carlo simulation, for the model estimates $x_{{\rm obs},i}$ corresponding to ω_0, ω_δ, and α. Minimizing χ^2 as a function of $\mathbf{r}$ near the expected locations leads us to the final estimates of the nuclear-spin position, indicated in Fig. 4. At these locations, we find a reduced chi-square of $\min_{\mathbf{r}}(\chi^2)/\nu = 2.7$ for both signs of $A_{||}$, where the degree of freedom $\nu = 12 - 3 = 9$ is based on the number of measurement variables (12) and fit parameters (three). The obtained value is not far from a reduced chi-square of 1 and the remaining inconsistency may be due to two reasons: first, the correction to the magnetic field is only a

first-order correction, which does not entirely resolve the discrepancy between the expected and measured splitting values; and, second, uncertainties in the reported g tensor itself [13] are not taken into account in our calculations.

3. Hydrogen concentration estimate

To consider the plausibility of the presence of hydrogen (H) in the YSO crystal, we provide an estimate of the H concentration. A confidence interval on the H concentration can be calculated based on our observation of H in the vicinity of one out of six total Er^{3+} ions studied in this sample. The purpose of this calculation is to provide a rough estimate of the concentration given available information.

The probability of observing some number k of hydrogen atoms within a given volume V and concentration ρ is described by the Poisson distribution: $P(k;\lambda) = (\lambda^k e^{-\lambda})/k!$, where $\lambda = \rho V$ is the expected number of H atoms in a given volume. Then, the probability of not observing hydrogen within the same volume is $P_0(\rho) = e^{-\rho V}$ and that of observing at least one H is $P_1(\rho) = 1 - P_0(\rho)$. Therefore, the probability of observing an H atom in the vicinity of n out of m Er^{3+} ions is $P(O|\rho) = \binom{n}{m} P_0(\rho)^{m-n} P_1(\rho)^n$. The probability distribution for the hydrogen concentration, constrained only by our observation, is then given by

$$p(\rho|O) = \frac{P(O|\rho)}{\int_0^\infty \mathrm{d}\rho' P(O|\rho')}, \tag{D5}$$

where we assume that the prior probability for the hydrogen concentration is uniform, i.e., $P(\rho) = P(\rho')$. The probability for the concentration to lie within a given range, (ρ_1, ρ_2), is then obtained by integrating the above expression: $P(\rho_1 \le \rho \le \rho_2|O) = \int_{\rho_1}^{\rho_2} p(\rho|O) d\rho$.

With one observation out of six trials ($n = 1, m = 6$), we obtain the probability distribution $p(\rho|O) = 30V(e^{-5\rho V} - e^{-6\rho V})$. We define the observable volume, $V = 4/3\pi r_{\mathrm{obs}}^3$, to be a sphere around the Er^{3+} ion. The observation of an H nuclear spin approximately 2 nm away from the Er^{3+} ion results in a near-full-contrast peak in the XY-16 sequence. However, farther-away H with weaker signals can also be observed provided that they are above the noise floor by a margin. To be 5σ above the noise floor at the resonant time, τ_0, we find that a conditional rotation of $N\alpha \simeq \pi/4$ is sufficient, in contrast to $N\alpha \simeq \pi$ for the observed interaction at $N = 16$ pulses for XY-16. The corresponding reduction in interaction strength, by a factor of approximately 4, allows for a hydrogen located farther away by a factor of approximately 1.5, or about 3 nm away from the Er^{3+} ion. Therefore, we set $r_{\mathrm{obs}} = 3$ nm for the observable volume. Based on the probability distribution, we find that the hydrogen concentration is in the range 0.3–3.9 $\times$ 10^{18} cm^{-3} with 68% confidence, with the most likely concentration at 1.6 $\times$ 10^{18} cm^{-3} (Fig. 7).

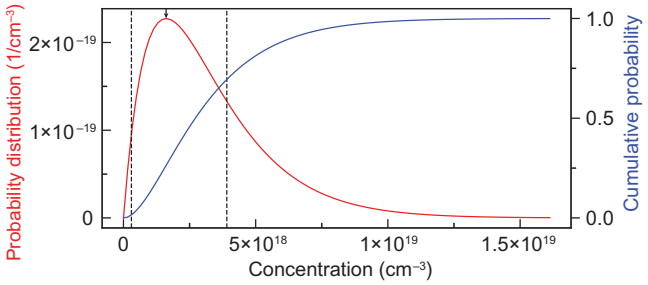

FIG. 7. Estimating the hydrogen concentration. The probability distribution for the hydrogen concentration, $p(\rho|O)$ (red), and the cumulative probability function $P(\rho|O) = \int_0^\rho p(\rho'|O)d\rho'$ (blue), as a function of the concentration in units of cm^{-3}. The dashed lines indicate the 68% confidence range from 0.3 $\times$ 10^{18} cm^{-3} to 3.9 $\times$ 10^{18} cm^{-3}. The probability distribution has a maximum at 1.6 $\times$ 10^{18} cm^{-3}.

APPENDIX E: NUCLEAR SPIN ENVIRONMENT

1. Nuclear spin coherence

We can try to understand the measured nuclear spin coherence (Fig. 2) in the context of the magnetic environment of the YSO host substrate, which consists of other nuclear spins and paramagnetic impurities. Because of its weak coupling to the environment, we can safely assume that the nuclear spin does not affect the dynamics of the surrounding spin bath. This allows us to discuss the nuclear spin decoherence as simply resulting from fluctuations of the spin bath. Following Ref. [45], we can represent the field applied by the bath as a time-dependent term, $\hat{\eta}_q(t)$, in the nuclear spin Hamiltonian:

$$H(t) = \omega_L I_z + \sum_{q=x,y,z} \hat{\eta}_q(t) I_q. \tag{E1}$$

To understand the pure dephasing of the nuclear spin, we work under the secular approximation for the nuclear spin, setting $\hat{\eta}_x = \hat{\eta}_y = 0$. To infer simple characteristics of the surrounding bath, we use the Gauss-Markov model, which assumes the correlation function $S(t) = \langle \eta'(t)\eta'(0)\rangle = \Delta^2 \exp(-|t|/\tau_b)$. Here, $\eta'(t)$ is a classical trajectory obtained by projecting the environmental variable $\hat{\eta}_z(t)$, Δ represents the amplitude of the fluctuations, and τ_b is the correlation time of the bath. Under the limit $\tau \ll \tau_b$, this model yields simple expressions for the Ramsey and Hahn coherence as $T_2^* = \sqrt{2}/\Delta$ and $T_{2,\mathrm{Hahn}} \sim (24\tau_b/\Delta^2)^{1/3}$.

We can extract a T_2^* for the nuclear spin by fitting an envelope of the form $\exp(-(\tau/T_2^*)^2)$ to the time-domain data of the Ramsey experiment [Fig. 2(b)], using the frequencies obtained from the FFT [Fig. 2(c)]. This yields a nuclear-spin T_2^* of 486 $\pm$ 20 μs. We would expect this value to scale with the gyromagnetic ratios, which are 15.2 MHz/G for the Er^{3+} spin at our field orientation and 4.26 kHz/G for the H nuclear spin. Based on our measurement

of the Er^{3+} Ramsey coherence $T_2^* = 115$ ns, this would lead to a hydrogen T_2^* of approximately 410 μs, which is close to the observed values. The difference may be due to the anisotropic g tensor of the Er^{3+} spin as well as uncertainty in determining the nuclear-spin T_2^* from the beating signal. Together with the measurement of $T_{2,\mathrm{Hahn}} = 1.9$ ms [Fig. 2(e)], this lets us extract a correlation time for the bath of $\tau_b \sim 2.4$ ms. The scaling of T_2 with the number of decoupling pulses, N', in the CPMG sequence is sublinear ($k = 0.5 \pm 0.1$) and not far from the scaling of $k = 2/3$ expected from this model under the stated assumptions. However, we note that the extracted correlation time is close to $T_{2,\mathrm{Hahn}}$, so the assumption $\tau \ll \tau_b$ may not be entirely valid. Furthermore, a simple relation between the nuclear-spin T_2 and the Er^{3+} -spin T_2 cannot be drawn because of the larger gyromagnetic ratio of the Er^{3+} spin, which implies that the bath dynamics will depend on the Er^{3+} state.

2. Discrete shifts in precession frequency

When measuring the free precession of the nuclear spin [Figs. 2(b) and 2(c)], we observe discrete shifts in the precession frequency of the nuclear spin. To explore this further, let us look at an example provided in Fig. 8(a) of the same experiment, where two different iterations of the experiment are out of phase with respect to each other, for the same precession times.

The frequencies are resolved in the FFT of the precession signal [Fig. 2(c)] and can be summarized as $\omega = \{\omega_0 + (-1)^i A_1 + (-1)^j A_2 : i,j \in (0,1)\}$, where ω_0 is the mean precession frequency and $A_1 = 2.25$ kHz and $A_2 = 7.18$ kHz are shifts in frequency. This motivates a simple model, where the nuclear spin interacts with two "dark spins," in the form $H_{\mathrm{dark}} = 2I_z(A_1 I_{z,d_1} + A_2 I_{z,d_2})$, where the precession frequency of the nuclear spin is shifted by $\pm A_1$ and $\pm A_2$ depending on the state of dark spins d_1 and d_2. Adding H_{dark} terms to the hyperfine-interaction Hamiltonian, we obtain the following four-body Hamiltonian:

$$\tilde{H} = 2S_z(A_{||}I_z + A_\perp I_x) + (\omega_L + 2A_1 I_{z,d_1} + 2A_2 I_{z,d_2})I_z. \tag{E2}$$

Using the above Hamiltonian, we can simulate the expected signal $s_0(\tau_c)_{ij}$ for a Ramsey experiment [Eq. (B15)], where the indices (i,j) corresponds to the dark-spin states that shift the precession frequency. In particular, we observe that curves with opposite d_2 states are roughly in phase with each other, while the d_1 state translates to a large phase offset, at the beginning of the time window in Fig. 8(b). This can be understood in terms of the phase difference accumulated due to d_1 and d_2 as a function of τ_c, $\phi_i(\tau_c) = 2A_i(\tau_c + 2N\tau_0)$ $(N = 8)$, where the second term is a correction due to the finite duration of the $C_n\mathrm{NOT}_e$ operation, during which the frequency of the nuclear spin is still shifted. This tells us that $\phi_2(\tau_c) = 2\pi$ at $\tau_c = 62.6$ μs, such that any population readout near this time window will be insensitive to the state of d_2.

Furthermore, the phase accumulated due to d_1 at $\tau_{c,1} = 72.19$ μs and $\tau_{c,2} = 73.14$ μs is as large as $\phi_1(\tau_c) \sim 0.7\pi$, such that the population is very sensitive to the d_1 state. Although larger phases can be accumulated for d_1 at later times, the d_2 state also becomes significant. Based on this model, we perform readout of d_1 by repeatedly measuring $s_0(\tau_c)$ at $\tau_{c,1}$ and $\tau_{c,2}$. In Fig. 9(a), we repeatedly perform the Ramsey experiment at times $\tau_{c,1}$ and $\tau_{c,2}$. At these times, we observe anticorrelated jumps in the signal that we attribute to quantum jumps of the d_1 state, as expected from Fig. 8(c). By thresholding based on a histogram of Fig. 9(b), we extract 98% readout fidelity for d_1 and extract

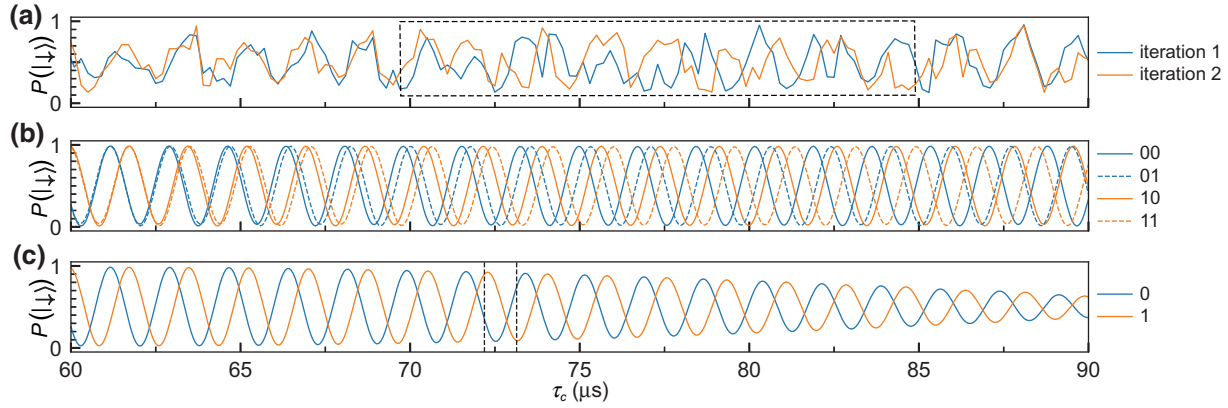

FIG. 8. Observing the frequency shifts. (a) The free-precession signal $s_0(\tau_c)$, which is expected to oscillate at ω_0, displays discrete shifts in frequency. This is manifested as a phase difference at the time scale above for two different iterations of the experiment. (b) The simulated precession signal $s_0(\tau_c)_{ij}$ for each scenario of the dark-spin pair initialization. (c) The simulated precession signal corresponding only to the d_1 state, after averaging over the d_2 states. Both readout locations (dashed lines) allow for distinguishing between d_1 states but with opposite populations.

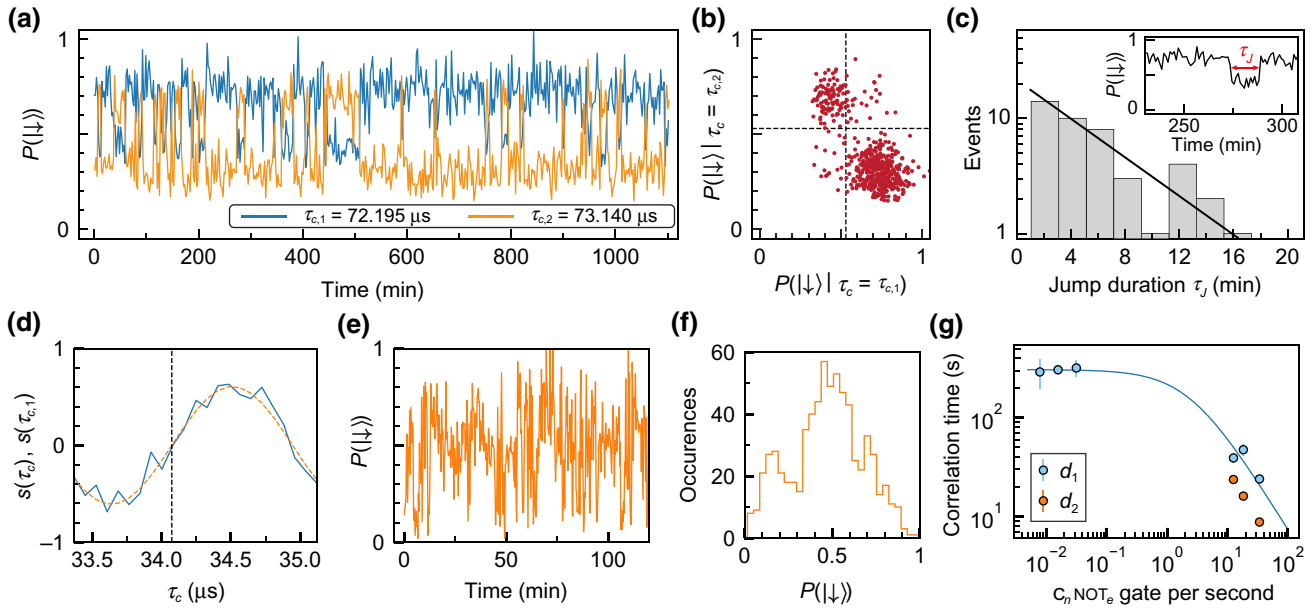

FIG. 9. The dark-spin readout. (a) Repeated Ramsey measurements at two different τ_c reveal quantum jumps of d_1. (b) The distribution of the measured populations in (a) are unequally weighted bimodally and anticorrelated at the two τ_c. (c) The duration of the quantum jumps shown in (a) is consistent with a lifetime of 5.19 ± 0.55 min (the black line is the fitted exponential decay). The inset shows a representative jump event from (a). (d) The cross-correlation measurement, comparing time traces equivalent to (a) at τ_c with the same at $\tau_{c,1}$ (where we observe d_1 jumps) in order to find a time point that is not correlated with the d_1 state. The vertical line indicates the point of no correlation with the d_1 state $\tau_c = 34.07$ μs. (e) Repetitive Ramsey measurements for d_2 performed at $\tau_c = 34.07$, displaying weaker-amplitude jumps. (f) The population histogram of d_2 extracted from (d). (g) The measured spin relaxation times at varying repetition rates of the $C_n NOT_e$ operation. At low repetition rates, the spin relaxation time approaches an intrinsic value $T_{1,\mathrm{dark}} = 5.12 \pm 0.13$ min for d_1.

its lifetime by looking at the frequency of jump events [Fig. 9(c)]. The measurement time (29 s) between consecutive data points in the Fig. 9(a) is small enough to observe d_1 jumps occurring with a lifetime of 5 min.

In order to observe d_2, we work at a value of τ_c that accumulates a phase for d_2 of $\phi_2(\tau_c) \sim 1.2\pi$, which is also uncorrelated with the d_1 state. Although d_1 already contributes an appreciable phase here, there still exist points in time where oscillations with a phase offset will intersect such that the population is insensitive to the d_1 state. The cross correlation of time traces $s(\tau_c)$ and $s(\tau_{c,1})$, yields a point of no correlation with the d_1 state, which we use to read out d_2 [Fig. 9(d)]. By performing faster measurements (every 5.9 s), we are able to observe quantum jumps associated with d_2, revealing a bimodal distribution [Figs. 9(e) and 9(f)]. The lifetimes associated with d_1 and d_2 reveal a dependency on the rate of the $C_n NOT_e$ operations applied [Fig. 9(g)], which suggests that d_1 and d_2 are perturbed by the probing of the nuclear spin.

As discussed in the main text, a direct interaction between the electron spin and the dark spins is investigated using a double electron-electron resonance (DEER) sequence [46] under the assumption that these are electron spins with $2 < g < 14$ but the spectroscopy does not reveal such interactions. We can verify that the shift in frequency is not due to a global effect, such as static magnetic field fluctuations, given the stable ground and excited spin resonance frequency of the Er^{3+} ion. Here, we propose two mechanisms to explain the frequency shift. d_1 and d_2 can be spin-1/2 nuclear spins in the YSO lattice: the hydrogen atom interacts with two nearby nuclear spins with interaction strengths of 2 kHz and 7 kHz, respectively. Alternatively, d_1 and d_2 could be represented by a single nuclear spin coupled to a tunneling hydrogen atom, such that the interaction strength modulates between 5 kHz and 9 kHz, due to relative changes in their position.

We expect that such a nuclear spin coupled to H may not be detectable directly via the Er^{3+} electron spin because of its finite coherence time. Based on Fig. 1(c), if we assume that we are able to resolve features up to approximately $3 \times 2\tau_{\mathrm{decay}} \simeq 3$ μs, this would indicate that we can resolve a Larmor frequency of 170 kHz (at $B = 130$ G), corresponding to a gyromagnetic ratio of 1.3 kHz/G. In particular, this precludes the detection of coherent signatures of the native Y or Si nuclear spins with gyromagnetic ratios of 0.84 kHz/G and 0.21 kHz/G, respectively.

We also note that an unidentified peak is observed around $2\tau = 1.5$ μs in Fig. 1(c). We investigate whether this peak could correspond to a nuclear spin that also interacts with H by various double-resonance techniques, but

are unable to observe a signal. Therefore, the origin of the peak at $2\tau = 1.5$ μs remains unknown.

In order to explore the origin of the local environment factors that cause the coupling of H with nearby nuclear spins, we perform DFT computation of H-related defect complexes in YSO and propose possible defects that can explain the frequency shift.

3. Density-functional-theory study of the origin of frequency shifts

Hydrogen is a ubiquitous impurity in semiconductors and insulators, as many growth and postgrowth processes introduce H. Here, we perform a systematic study of the structure and formation energies of hydrogen-related centers in YSO. Hydrogen can be present as hydrogen interstitials or as substitutional H (H_O) and can also form complexes with impurities or with vacancies. We consider impurities that have nonzero nuclear spin and that based on chemical analysis are expected to be present in the sample: applying these criteria, we focus on Cd_Y and P_O, which act as acceptors and can form complexes with H.

Our DFT calculations are performed using the projector augmented-wave method implemented in the Vienna *ab initio* simulation package (VASP) [47,48]. The plane-wave cutoff energy is 500 eV. The hybrid exchange-correlation functional of Heyd, Scuseria, and Ernzerhof (HSE) [49] is used with 25% mixing of Hartree-Fock exchange, which yields the direct band gap of 6.49 eV, in reasonable agreement with the experimental band gap (6.14 eV) [50]. The computed lattice constants of YSO are $a = 14.40$ Å, $b = 6.75$ Å, $c = 10.44$ Å, and $\beta = 122.1°$, in very good agreement with the experimental values ($a = 14.37$ Å, $b = 6.71$ Å, $c = 10.40$ Å, and $\beta = 122.2°$) [51].

The crystal structure of YSO (with $C/2m$ space-group symmetry) is sketched in Fig. 10(a). YSO has two types of Y atoms (Y_I and Y_{II}), one type of Si atom, and five types of O atoms (O_I, O_{II}, O_{III}, O_{IV}, and O_V). Figure 10(b) summarizes the coordination of the Y, Si, and O atoms. To calculate defect structures, we construct a supercell with dimensions $a \times 2b \times c$, containing 128 atoms. We consider the following defect structures that could involve H interacting with cations that have nuclear spin 1/2: H interstitials (H_i), substitutional hydrogen (which can also be viewed as an oxygen vacancy−H complex) (H_O), Si vacancy−H complex (V_{Si}-H), Y vacancy−H complex (V_Y-H), substitutional Cd−substitutional H complex (Cd_Y-H_O), and substitutional P−H complex (P_O-H).

The formation energy $E^f(D^q)$ of a point defect D in charge state q is calculated as

$$E^f(D^q) = E(D^q) - E_{\text{bulk}} + \sum \mu_i n_i + qE_F + \Delta_{\text{corr}}. \tag{E3}$$

$E^f(D^q)$ is the total energy of the supercell containing defect D in the charge state q. E_{bulk} is the total energy of the perfect supercell. $|n_i|$ is the number of atoms added ($n_i < 0$) or removed ($n_i > 0$) from the system. μ_i is the chemical potential of species i and E_F is the Fermi level, which is referenced to the valence-band maximum (VBM). Δ_{corr} is a term that corrects for the finite size of charged supercells.

We define $\Delta\mu_i$ as the deviation of the chemical potential from the reference states: $\mu_i = \mu_{i,\text{ref}} + \Delta\mu_i$. For Y (Si), $\mu_{i,\text{ref}}$ is the energy of bulk Y (Si) and for oxygen, the reference is an O_2 molecule. Assuming thermodynamic equilibrium, the $\Delta\mu_i$ are related by

$$2\Delta\mu_Y + \Delta\mu_{Si} + 5\Delta\mu_O = \Delta H^f(Y_2SiO_5). \tag{E4}$$

$\Delta H^f(Y_2SiO_5)$ is the formation enthalpy of YSO. The $\Delta\mu_i$ are also limited by the formation of other compounds: $2\Delta\mu_Y + 3\Delta\mu_O < \Delta H^f(Y_2O_3)$, $\Delta\mu_{Si} + 2\Delta\mu_O < \Delta H^f(SiO_2)$, and $2\Delta\mu_H + \Delta\mu_O < \Delta H^f(H_2O)$. $\Delta H^f(Y_2O_3) = -19.23$ eV, $\Delta H^f(SiO_2) = -8.97$ eV, and $\Delta H^f(H_2O) = -2.65$ eV are the formation enthalpies of Y_2O_3, SiO_2, and H_2O. The constraints imposed by Y_2O_3, SiO_2, and H_2O define a stability region for YSO, which is shown in Fig. 11(a). We choose to use the O-rich, Si-rich [Fig. 11(b)] and O-poor, Si-rich [Fig. 11(c)] conditions to present the formation energies.

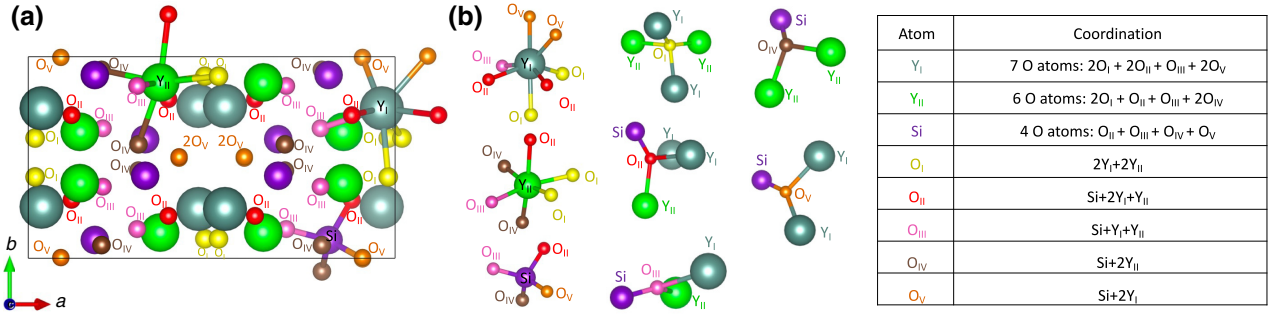

FIG. 10. (a) The structure of Y_2SiO_5 (YSO). The unit cell is indicated and contains 64 atoms. (b) The coordination of Y, Si, and O atoms in Y_2SiO_5.

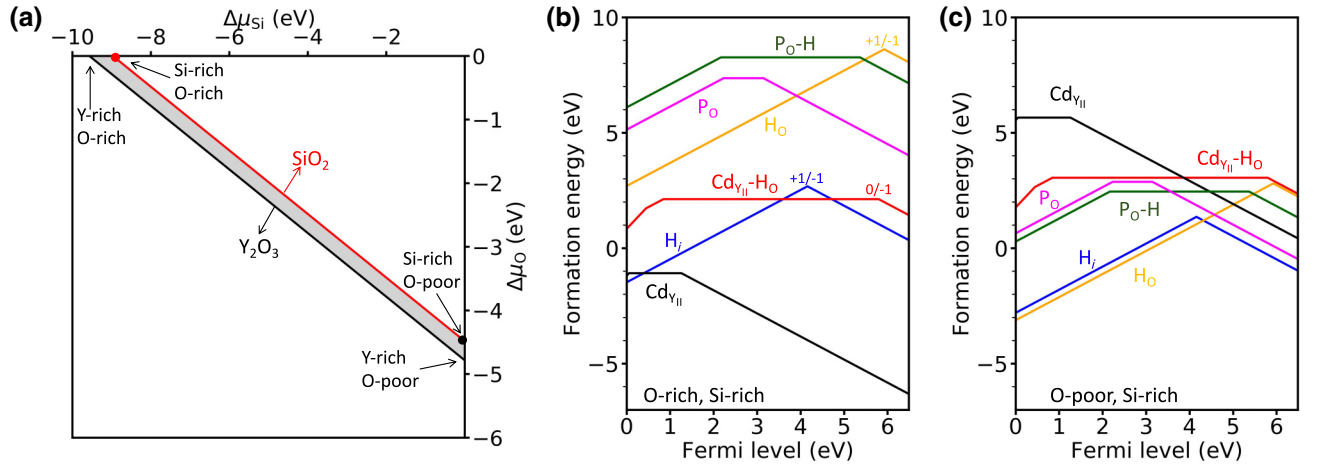

FIG. 11. (a) The stability region for Y_2SiO_5, shaded in gray. The red (O-rich, Si-rich) and black (O-poor, Si-rich) dots represent the choice of chemical potentials in this study. (b),(c) The formation-energy diagram of defects under (b) O-rich, Si-rich and (c) O-poor, Si-rich (c) conditions.

We then focus on identifying hydrogen positions that would be consistent with the observed frequency shifts of 2 kHz and 7 kHz resulting from interaction with a spin-1/2 nucleus. From the two-body magnetic dipole interaction Hamiltonian, we calculate the frequency shift as

$$A = \frac{1}{2}\frac{\mu_0\mu_N^2 g_1 g_2}{4\pi r^3}\left(1-3\cos^2\theta\right), \tag{E5}$$

where μ_N is the nuclear magneton, μ_0 is the magnetic constant, g_1 and g_2 are the nuclear-spin g factors, r is the distance between the two nuclei, and θ is the angle between the bond and the magnetic field. The maximum shift is obtained when the magnetic field is aligned with the bond direction.

First, we examine whether interstitial or substitutional hydrogen interacting with host atoms (Y or Si) could be responsible for the observed frequency shifts. The bottleneck, caused by the small nuclear-spin g factor of Y, is the identification of a location where H can be close enough to an Y atom to yield a 2-kHz frequency shift. After examining many configurations, we find that the shortest H—Y distance is found in H_O in a +1 charge state (H_O^+) [Fig. 12(a)]. The corresponding H—Si distance is 1.5 Å. The H—Si distance of 1.5 Å can lead to a 7-kHz frequency shift; but even the short H—Y distance (2.4 Å) leads to a frequency shift of only 0.4 kHz. Hydrogen interacting with Y and Si atoms thus cannot explain the observed frequency shifts.

We therefore consider interactions of hydrogen with unintentional impurities, for which Cd and P are prime candidates. After extensive exploration of possible configurations, we propose the following two defect complexes that yield magnetic coupling strengths in the vicinity of observed values: Cd_Y-H_O [Fig. 12(b)] and P_O-H_i [Fig. 12(c)].

Cd_Y-H_O [Fig. 12(b)] with a Y_{II} atom substituted by a Cd atom and an O_{IV} atom substituted by a H atom is stable in the neutral charge state over a wide range of the Fermi level. The formation energy is 2.12 eV under O-rich, Si-rich conditions and 3.05 eV under O-poor, Si-rich conditions. The binding energy, calculated as $E_{\text{bind}} = E^f(\text{Cd}_{\text{Y}_{\text{II}}}) + E^f(\text{H}_{\text{O}_{\text{IV}}}) - E^f(\text{Cd}_\text{Y}\text{-H}_\text{O})$, is positive (0.76 eV), which indicates that the defect complex is more stable than spatially separated $Cd^-_{Y_{II}}$ and H^+_O. The H—Cd distance is 2.4 Å and the H—Si distance is 1.5 Å. The largest frequency shifts that these distances allow, assuming that the field is aligned with the bonds, are 2 kHz for H—^{111}Cd coupling and 7 kHz for H—^{29}Si coupling. However, the Cd—H–Si bond angle of 120° implies that the magnetic field cannot be simultaneously aligned with each bond, yielding smaller interaction strengths for a given field direction. For instance, if we assume that the angle between the magnetic field and the H—Cd bond is 35° and that it is 155° for the H—Si bond, then the H—Cd coupling is 1.7 kHz and the H—Si coupling is 4.9 kHz.

P_O-H_i [Fig. 12(c)] is also stable in the neutral charge state over a wide range of the Fermi level. The formation energy is 2.45 eV under O-poor, Si-rich conditions. The defect complex is also more stable than separated $P^-_{O_{IV}}$ and H_i^+, with $E_{\text{bind}} = 0.85$ eV. The H—Si distance is 2.2 Å, leading to a maximum coupling strength of 2 kHz when the field is aligned with the bond. The H—P distance is 1.4 Å and due to the g factor of P being much larger than that of Si, this leads to a maximum coupling strength of 17 kHz. Since the P—H—Si angle is 69°, taking the alignment of the magnetic field into account similarly lowers the H—P coupling. For instance, assuming that the angle between the magnetic field and the bond is 10° for the H—Si bond and 79° for the H—P bond, the H—Si coupling is still 2 kHz but the H—P coupling is 7 kHz. Therefore, a field

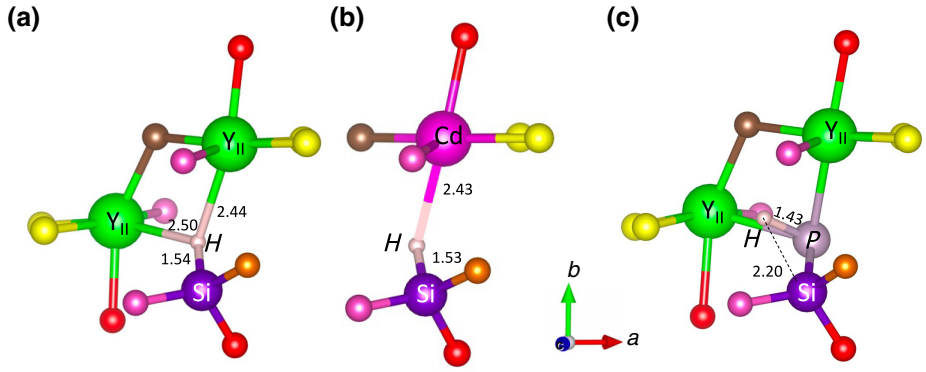

FIG. 12. The structures of defect complexes: (a) $H_{O_{IV}}$ at $q = +1$, (b) Cd_Y-H_O, and (c) P_O-H_i.

direction exists such that the P_O-H_i complex yields the coupling strengths observed in the experiment. However, the required magnetic field direction does not match the field direction set in the experiment within error. At our field direction, we expect this complex to yield an H—Si coupling of 0.5 kHz and a H—P coupling of 7.5 kHz.

We note that hydrogen can often occupy several inequivalent positions in the vicinity of the impurity with similar energies; some of these positions could lead to alignments or distances that yield coupling strengths with even closer agreement. Our calculations for the Cd_Y-H_O and P_O-H_i complexes show that the observed frequency shifts can plausibly be due to interactions within such defect complexes.

[1] S. Wehner, D. Elkouss, and R. Hanson, Quantum Internet: A vision for the road ahead, Science **362**, eaam9288 (2018).

[2] C. L. Degen, F. Reinhard, and P. Cappellaro, Quantum sensing, Rev. Mod. Phys. **89**, 035002 (2017).

[3] D. D. Awschalom, R. Hanson, J. Wrachtrup, and B. B. Zhou, Quantum technologies with optically interfaced solid-state spins, Nat. Photon. **12**, 516 (2018).

[4] F. Jelezko, T. Gaebel, I. Popa, M. Domhan, A. Gruber, and J. Wrachtrup, Observation of Coherent Oscillation of a Single Nuclear Spin and Realization of a Two-Qubit Conditional Quantum Gate, Phys. Rev. Lett. **93**, 130501 (2004).

[5] L. Childress, M. Gurudev Dutt, J. Taylor, A. Zibrov, F. Jelezko, J. Wrachtrup, P. Hemmer, and M. Lukin, Coherent dynamics of coupled electron and nuclear spin qubits in diamond, Science **314**, 281 (2006).

[6] P. Neumann, N. Mizuochi, F. Rempp, P. Hemmer, H. Watanabe, S. Yamasaki, V. Jacques, T. Gaebel, F. Jelezko, and J. Wrachtrup, Multipartite entanglement among single spins in diamond, Science **320**, 1326 (2008).

[7] P. C. Maurer, G. Kucsko, C. Latta, L. Jiang, N. Y. Yao, S. D. Bennett, F. Pastawski, D. Hunger, N. Chisholm, and M. Markham, *et al.*, Room-temperature quantum bit memory exceeding one second, Science **336**, 1283 (2012).

[8] W. Pfaff, B. J. Hensen, H. Bernien, S. B. van Dam, M. S. Blok, T. H. Taminiau, M. J. Tiggelman, R. N. Schouten, M. Markham, D. J. Twitchen, and R. Hanson, Unconditional quantum teleportation between distant solid-state quantum bits, Science **345**, 532 (2014).

[9] T. H. Taminiau, J. Cramer, T. van der Sar, V. V. Dobrovitski, and R. Hanson, Universal control and error correction in multi-qubit spin registers in diamond, Nat. Nanotechnol. **9**, 171 (2014).

[10] G. Waldherr, Y. Wang, S. Zaiser, M. Jamali, T. Schulte-Herbrüggen, H. Abe, T. Ohshima, J. Isoya, J. Du, and P. Neumann, *et al.*, Quantum error correction in a solid-state hybrid spin register, Nature **506**, 204 (2014).

[11] J. Cramer, N. Kalb, M. A. Rol, B. Hensen, M. S. Blok, M. Markham, D. J. Twitchen, R. Hanson, and T. H. Taminiau, Repeated quantum error correction on a continuously encoded qubit by real-time feedback, Nat. Commun. **7**, 11526 (2016).

[12] M. H. Abobeih, Y. Wang, J. Randall, S. J. H. Loenen, C. E. Bradley, M. Markham, D. J. Twitchen, B. M. Terhal, and T. H. Taminiau, Fault-tolerant operation of a logical qubit in a diamond quantum processor, Nature **606**, 884 (2022).

[13] Y. Sun, T. Böttger, C. Thiel, and R. Cone, Magnetic g tensors for the $^4I_{15/2}$ and $^4I_{13/2}$ states of Er^{3+}:Y_2SiO_5, Phys. Rev. B **77**, 085124 (2008).

[14] P. Siyushev, K. Xia, R. Reuter, M. Jamali, N. Zhao, N. Yang, C. Duan, N. Kukharchyk, A. Wieck, and R. Kolesov, *et al.*, Coherent properties of single rare-earth spin qubits, Nat. Commun. **5**, 3895 (2014).

[15] T. Utikal, E. Eichhammer, L. Petersen, A. Renn, S. Götzinger, and V. Sandoghdar, Spectroscopic detection and state preparation of a single praseodymium ion in a crystal, Nat. Commun. **5**, 3627 (2014).

[16] I. Nakamura, T. Yoshihiro, H. Inagawa, S. Fujiyoshi, and M. Matsushita, Spectroscopy of single Pr^{3+} ion in LaF_3 crystal at 1.5 K, Sci. Rep. **4**, 7364 (2014).

[17] A. Dibos, M. Raha, C. Phenicie, and J. D. Thompson, Atomic Source of Single Photons in the Telecom Band, Phys. Rev. Lett. **120**, 243601 (2018).

[18] T. Zhong, J. M. Kindem, J. G. Bartholomew, J. Rochman, I. Craiciu, V. Verma, S. W. Nam, F. Marsili, M. D. Shaw, and A. D. Beyer, *et al.*, Optically Addressing Single Rare-Earth Ions in a Nanophotonic Cavity, Phys. Rev. Lett. **121**, 183603 (2018).

[19] A. Ulanowski, B. Merkel, and A. Reiserer, Spectral multiplexing of telecom emitters with stable transition frequency, Sci. Adv. **8**, eabo4538 (2022).

[20] M. Raha, S. Chen, C. M. Phenicie, S. Ourari, A. M. Dibos, and J. D. Thompson, Optical quantum nondemolition measurement of a single rare earth ion qubit, Nat. Commun. **11**, 1605 (2020).

[21] J. M. Kindem, A. Ruskuc, J. G. Bartholomew, J. Rochman, Y. Q. Huan, and A. Faraon, Control and single-shot readout of an ion embedded in a nanophotonic cavity, Nature **580**, 201 (2020).

[22] S. Chen, M. Raha, C. M. Phenicie, S. Ourari, and J. D. Thompson, Parallel single-shot measurement and coherent control of solid-state spins below the diffraction limit, Science **370**, 592 (2020).

[23] T. Zhong and P. Goldner, Emerging rare-earth doped material platforms for quantum nanophotonics, Nanophotonics **8**, 2003 (2019).

[24] C. M. Phenicie, P. Stevenson, S. Welinski, B. C. Rose, A. T. Asfaw, R. J. Cava, S. A. Lyon, N. P. De Leon, and J. D. Thompson, Narrow optical line widths in erbium implanted in TiO_2, Nano Lett. **19**, 8928 (2019).

[25] P. Stevenson, C. M. Phenicie, I. Gray, S. P. Horvath, S. Welinski, A. M. Ferrenti, A. Ferrier, P. Goldner, S. Das, and R. Ramesh, *et al.*, Erbium-implanted materials for quantum communication applications, Phys. Rev. B **105**, 224106 (2022).

[26] C. Yin, M. Rancic, G. G. de Boo, N. Stavrias, J. C. McCallum, M. J. Sellars, and S. Rogge, Optical addressing of an individual erbium ion in silicon, Nature **497**, 91 (2013).

[27] S. Ourari, L. Dusanowski, S. P. Horvath, M. T. Uysal, C. M. Phenicie, P. Stevenson, M. Raha, S. Chen, R. J. Cava, N. P. de Leon, and J. D. Thompson, Indistinguishable telecom band photons from a single erbium ion in the solid state, (2023), ArXiv:2301.03564.

[28] G. Liu and B. Jacquier, *Spectroscopic Properties of Rare Earths in Optical Materials* (Springer-Verlag, Berlin, 2005).

[29] T. Kornher, D.-W. Xiao, K. Xia, F. Sardi, N. Zhao, R. Kolesov, and J. Wrachtrup, Sensing Individual Nuclear Spins with a Single Rare-Earth Electron Spin, Phys. Rev. Lett. **124**, 170402 (2020).

[30] A. Ruskuc, C.-J. Wu, J. Rochman, J. Choi, and A. Faraon, Nuclear spin-wave quantum register for a solid-state qubit, Nature **602**, 408 (2022).

[31] N. Kalb, P. C. Humphreys, J. Slim, and R. Hanson, Dephasing mechanisms of diamond-based nuclear-spin memories for quantum networks, Phys. Rev. A **97**, 062330 (2018).

[32] A. Reiserer, N. Kalb, M. S. Blok, K. J. van Bemmelen, T. H. Taminiau, R. Hanson, D. J. Twitchen, and M. Markham, Robust Quantum-Network Memory Using Decoherence-Protected Subspaces of Nuclear Spins, Phys. Rev. X **6**, 021040 (2016).

[33] S. Chen, S. Ourari, M. Raha, C. M. Phenicie, M. T. Uysal, and J. D. Thompson, Hybrid microwave-optical scanning probe for addressing solid-state spins in nanophotonic cavities, Opt. Express **29**, 4902 (2021).

[34] S. Kolkowitz, Q. P. Unterreithmeier, S. D. Bennett, and M. D. Lukin, Sensing Distant Nuclear Spins with a Single Electron Spin, Phys. Rev. Lett. **109**, 137601 (2012).

[35] T. Taminiau, J. Wagenaar, T. Van der Sar, F. Jelezko, V. V. Dobrovitski, and R. Hanson, Detection and Control of Individual Nuclear Spins Using a Weakly Coupled Electron Spin, Phys. Rev. Lett. **109**, 137602 (2012).

[36] N. Zhao, J. Honert, B. Schmid, M. Klas, J. Isoya, M. Markham, D. Twitchen, F. Jelezko, R.-B. Liu, and H. Fedder, *et al.*, Sensing single remote nuclear spins, Nat. Nanotechnol. **7**, 657 (2012).

[37] C. G. Van de Walle and J. Neugebauer, Universal alignment of hydrogen levels in semiconductors, insulators and solutions, Nature **423**, 626 (2003).

[38] M. D. McCluskey, M. C. Tarun, and S. T. Teklemichael, Hydrogen in oxide semiconductors, J. Mater. Res. **27**, 2190 (2012).

[39] G. A. Shi, M. Saboktakin, M. Stavola, and S. Pearton, "Hidden hydrogen" in as-grown ZnO, Appl. Phys. Lett. **85**, 5601 (2004).

[40] D. Devor, R. Pastor, and L. DeShazer, Hydroxyl impurity effects in YAG ($Y_3Al_5O_{12}$), J. Chem. Phys. **81**, 4104 (1984).

[41] S. Mu, M. Wang, J. B. Varley, J. L. Lyons, D. Wickramaratne, and C. G. Van de Walle, Role of carbon and hydrogen in limiting *n*-type doping of monoclinic $(Al_xGa_{1-x})_2O_3$, Phys. Rev. B **105**, 155201 (2022).

[42] T. Van der Sar, Z. Wang, M. Blok, H. Bernien, T. Taminiau, D. Toyli, D. Lidar, D. Awschalom, R. Hanson, and V. Dobrovitski, Decoherence-protected quantum gates for a hybrid solid-state spin register, Nature **484**, 82 (2012).

[43] C. E. Bradley, J. Randall, M. H. Abobeih, R. C. Berrevoets, M. J. Degen, M. A. Bakker, M. Markham, D. J. Twitchen, and T. H. Taminiau, A Ten-Qubit Solid-State Spin Register with Quantum Memory up to One Minute, Phys. Rev. X **9**, 031045 (2019).

[44] M. Le Dantec, M. Rančić, S. Lin, E. Billaud, V. Ranjan, D. Flanigan, S. Bertaina, T. Chanelière, P. Goldner, and A. Erb, *et al.*, Twenty-three–millisecond electron spin coherence of erbium ions in a natural-abundance crystal, Sci. Adv. **7**, eabj9786 (2021).

[45] R. de Sousa, in *Electron Spin Resonance and Related Phenomena in Low-Dimensional Structures* (Springer-Verlag, Berlin, 2009).

[46] M. Degen, S. Loenen, H. Bartling, C. Bradley, A. Meinsma, M. Markham, D. Twitchen, and T. Taminiau, Entanglement of dark electron-nuclear spin defects in diamond, Nat. Commun. **12**, 3470 (2021).

[47] G. Kresse and J. Furthmüller, Efficient iterative schemes for *ab initio* total-energy calculations using a plane-wave basis set, Phys. Rev. B **54**, 11169 (1996).

[48] G. Kresse and J. Furthmüller, Efficiency of ab-initio total energy calculations for metals and semiconductors using a plane-wave basis set, Comput. Mater. Sci. **6**, 15 (1996).

[49] J. Heyd, G. E. Scuseria, and M. Ernzerhof, Hybrid functionals based on a screened Coulomb potential, J. Chem. Phys. **118**, 8207 (2003).

[50] H. Pang, G. Zhao, M. Jie, J. Xu, and X. He, Study on the growth, etch morphology and spectra of Y_2SiO_5 crystal, Mater. Lett. **59**, 3539 (2005).

[51] H. M. O'Bryan, P. K. Gallagher, and G. Berkstresser, Thermal expansion of Y_2SiO_5 single crystals, J. Am. Ceram. Soc. **71**, C42 (1988).